

**STRUCTURAL INVESTIGATION OF COPOLYMERIZATION REACTIONS IN
RESTRICTED DIMENSIONS**

By

CRYSTIANA WHEELWRIGHT

**A DISSERTATION PRESENTED TO THE GRADUATE SCHOOL
OF THE UNIVERSITY OF FLORIDA IN PARTIAL FULFILLMENT
OF THE REQUIREMENTS FOR THE DEGREE OF
DOCTOR OF PHILOSOPHY**

UNIVERSITY OF FLORIDA

2008

This dissertation is dedicated to my parents, Demetris Wemmers and Hazel Wemmers, for their love and support.

ACKNOWLEDGEMENTS

I would like to express my sincere appreciation to my mentor, Dr. Randy Dumas, for his guidance and friendship over the last five years. I would like to thank all the members of the Dumas Research Group and the Oxygen and Isotopes (Oxide-Polymer) Research Laboratory for their friendship and help and for making the Polymer Group an enjoyable place to work.

Financial and technical support was given by The Petroleum Research Fund (I1442-8C7), Graduate Research Assistantship Program granted by Development Sponsored Research at University of Florida, NSF Instruments of Finland, and Marwood Software. I would like to acknowledge Paula Dunn, Mary Gustin, Ashwary Datta, and Jim Kautler from Northwestern University and Stefan Leyenswaka, Andrew King, and Bill Lousader from MRCAT, Argonne National Laboratories for their help and guidance during the spectroscopic experiments. Special thanks to Peter Veedriem who translated the LD film and ran X-ray experiments with me and to Jeffrey Culp and Stefan Jato who ran 2D-T synchronous X-ray experiments with me. Thanks to David Powell, Doug Schoenfeld, John Johnson, Beth Tran, and Chris Szabicki for spending their valuable time running my samples to obtain meaningful mass spectrometry data.

My appreciation also goes to my friends at Georgia College who created me with love and made me feel at home. My Special thanks to David Banta, Elizabeth Banta, Betty LeDoux, Bill Lantz, Dana Moody, Margaret Delgado, Christopher Rynish, Michael Thirumal, Indira Thirumal, and Dharmendra Chaturvedi who maintained me in

Georgetown College. Allow my thanks go to my close friends, Indira and Dennis Tamers, for their constant and support. I thank my friends at the University of Florida, Chung, Hiron, Muzil, Francis, and Ben, who have shown me the true role of college life. I must thank my best friends at the University of Florida, Stephanie Barnabach and Leslie King, who were there for me during all kinds of weather. My thanks to Barbara Stange for offering the text.

My family has always been the real hope behind my accomplishments. I am very fortunate to have my father, mother, and two brothers, Joshua and Paul, to believe that I can succeed. I cannot begin to express how much their love and support mean to me. I would also like to give a very special thank you to Henna Wismadarsa who supported me financially during my undergraduate studies. I would not be here without her support. Thank you for having faith in me.

Finally, I would like to thank the wonderful staff of the Chemistry Department including Lorraine Williams, Joe Shinsky, Todd Price, Joe Connors, Lawrence Herley, and Michael Weststrate. Special thanks to Lou Clark, Deane Bellum, and Jim Dwyer of the graduate program office for helping me with all the problems that graduate students have to face.

TABLE OF CONTENTS

page

ACKNOWLEDGEMENTS	ii
LIST OF TABLES	vii
LIST OF FIGURES	ix
ABSTRACT	xvi
CHAPTERS	
1. INTRODUCTION	1
1.1 Langmuir and Langmuir-Blodgett Films	1
1.1.1 History of Langmuir and Langmuir-Blodgett Films	2
1.1.2 Basic Concepts of Langmuir Monolayers	4
1.1.3 Monolayer Film Dependence on its Solid Substrate	9
1.1.4 Polymerization at the Air/Water Interface	12
1.2 Thermodynamics of the Langmuir Monolayers	13
1.2.1 Two-dimensional Expansion of State	15
1.2.2 Monolayer Phase Transitions	18
1.2.3 Mixed Monolayers	17
1.3 Mass Spectrometry	19
1.3.1 Overview of MALDI	20
1.3.2 Overview of ESI	22
1.3.3 Overview of APCI	23
1.3.4 Current Usage of MALDI, APCI, and ESI in Polymer	24
1.4 Scopy Definition	26
1.5 Applications of Langmuir and Langmuir-Blodgett Films	29
1.6 Conclusion	37
2. CHARACTERIZATION OF THE LANGMUIR FILMS	39
2.1 Introduction	39
2.2 Experimental Procedures	39
2.2.1 Langmuir and Langmuir-Blodgett Films	39
2.2.1.1 Langmuir Graph	40
2.2.1.2 Monolayer Thickness	42
2.2.1.3 Surface mobility	43

2.2.1.4 Hysteresis	41
2.2.1.5 Langmuir-Blodgett films	44
2.2.1.6 Surface potential	48
2.2.1.7 Polymerization at the interface	49
2.2.1.8 Brewster Angle Microscopy	49
2.2.2 UV-Vis Spectroscopy	48
2.2.3 IR Spectroscopy	48
2.2.4 NMR Spectroscopy	48
2.2.5 Gel Permeation Chromatography	48
2.3 Minerals	49
2.3.1 Nitro-activated Pyrolysis	49
2.3.2 Nitro-activated Pyrolysis	49
2.3.3 Cleaning Procedures	54
2.3.4 Solvents Properties	57
2.3.5 Solid Solvents Preparation	58
2.4 Langmuir Monolayer Characterization	59
2.4.1 Isotherms	59
2.4.2 Isotherm Stability	64
2.4.3 Expansion	65
2.4.4 Compressibility and Pseudo Area of Mixing	67
2.4.5 Brewster Angle Microscopy	69
2.4.6 Surface Pressure	69
2.4.7 Langmuir-Blodgett Films	72
2.5 Langmuir Monolayer Polymerization	73
2.6 Characterization by Standard Polymer Techniques	77
2.6.1 UV-Vis Spectroscopy	77
2.6.2 IR Spectroscopy	79
2.6.3 NMR Spectroscopy	81
2.6.4 Gel Permeation Chromatography	81
2.7 Conclusions	82
3 MASS SPECTROMETRY OF POLYMERIC MATERIALS	84
3.1 Introduction	85
3.2 Experimental Procedures	89
3.2.1 MALDI-TOF Experiments	89
3.2.1.1 Sample preparation	89
3.2.1.2 Mass spectrometry	90
3.2.2 LC-MS Experiments	95
3.2.2.1 Sample preparation	95
3.2.2.2 Mass spectrometry	95
3.3 Results and Discussion	98
3.3.1 MALDI-TOF-MS	98
3.3.2 LC-APCI-MS	97
3.4 Conclusions	102

4 X-RAY DIFFRACTION OF LANGMUIR AND LANGMUIR-BLODGETT FILMS	
4.1 Introduction	104
4.2 Experimental Procedure	105
4.2.1 Powder Definition of Measurement of XRD and XGOF	106
4.2.2 X-ray Definition of Langmuir-Blodgett Films	107
4.2.3 X-ray Definition of Langmuir Films at Air/Water Interface	108
4.2.3.1 Diffraction against	109
4.2.3.2 Alignment	114
4.3 Results and Discussion	118
4.3.1 Powder Definition of the Monolayer	118
4.3.2 Grazing Incidence X-ray Definition of the Langmuir-Blodgett Films	119
4.3.3 Grazing Incidence X-ray Definition of the Langmuir Films	120
4.4 Conclusion	126
5 CONSTRUCTION OF THE INSTRUMENTATION FOR GRAZING INCIDENCE X-RAY DIFFRACTION	129
5.1 Introduction	129
5.2 Instrumentation	129
5.2.1 Vertical Defining Mirror	132
5.2.2 The Langmuir Torque	134
5.2.3 X-ray Detector	144
5.3 Results and Discussion	148
5.4 Conclusion	154
APPENDICES	
A. CALCULATION OF HORIZONTAL BOND LENGTHS OF A DISTORTED HEXAGONAL LATTICE	163
B. EXPERIMENT SETUP CHECKLIST FOR ALIGNMENT PROTOCOLS FOR GRAZING INCIDENCE DIFFRACTION OF LANGMUIR MONOLAYERS AT THE MARCAT BEAMLINE	167
C. MECHANICAL DIMENSIONS OF DIFFERENT COMPONENTS WHICH WERE USED IN THE GIXD EXPERIMENT	159
REFERENCES	164
BIOGRAPHICAL SKETCH	174

LIST OF TABLES

Table	Page
1-1 Sizes of the spinel-type oxides around the world.	19
1-2 Properties and applications of LD films.	36
2-1 Important values extracted from Figure 2-2.	61
2-2 Important values extracted from Figure 2-4.	62
3-1 Peak positions and the peak assignments of some selected peaks of the MALDI-TOF spectra in Figure 3-5.	93
3-2 Peak positions and the peak assignments of some selected peaks of the MALDI-TOF spectra in Figure 3-6.	97
4-1 Data obtained from the powder diffraction of HDEP.	117
4-2 Data obtained from the powder diffraction of HDEP.	118
4-3 Data obtained from the GED of Langmuir-Blodgett films.	125
4-4 Summarized information of several different GED setups.	143

LIST OF FIGURES

Figure	Page
1-1 Surface pressure versus area per molecule (system for a long chain organic compound and the corresponding molecular arrangement) of the monolayer	4
1-2 Diagram (not in scale) showing forces acting on the Wilhelmy plate	7
1-3 Diagrams types of LB films	8
1-4 Transferring on T-type LB molecule from a hydrophobic surface	11
1-5 General mechanism for the oscillatory polymerization of pyridine	14
1-6 Spectral brilliance of some X-ray sources	25
1-7 Geometry of a plane X-ray diffraction	31
1-8 View of the monolayer and the corresponding intensity distribution tilted phase	34
2-1 ILS/NOO Langmuir trough system with a sapphire and surface Brillouin scatter attached	40
2-2 Schematic of the setup for measuring surface potential by vibrating plate method	43
2-3 Schematic of Brewster Angle Microscopy	47
2-4 Synthetic route to 3-ferrocenyl pyridine	51
2-5 ^1H NMR spectra of monomers	53
2-6 ^{13}C NMR spectra of monomers	56
2-7 Monolayer molecular of 3-ferrocenyl pyridine on ZPC	60
2-8 Isolation of monomers of 3-ferrocenyl pyridine at different temperatures	63
2-9 Synthesis of the polymerized monolayer product of 3-ferrocenyl pyridine	64

2-10	Success rate of coating on CPC	60
2-11	Dependence of temperature and mole fraction on compressibility of $\text{C}_{12}\text{H}_{25}\text{NMe}_3\text{Br}$	61
2-12	RAFM images of HQEP	63
2-13	Surface potential of monomers of CPC	70
2-14	Surface dipole moment corresponding to zero surface pressure	71
2-15	Langmuir-Blodgett transfer of 3-benzodicyl pyrrole onto hydrophobized silica wafers	71
2-16	Isolation of polymer after coating on $\text{C}_{12}\text{-C}_{20}\text{H}_{41}\text{NMe}_3\text{Br}$ and CPC	74
2-17	Polymerization of pure SHEP at 25°C	75
2-18	Polymerization of 50% mixture of SHEP and HQEP at 25°C	76
2-19	UV-vis spectra of (a) 3-benzodicyl pyrrole and (b) its polymerization product from the LB trough in dichloroform solution	78
2-20	IR spectrum of (a) 3-benzodicyl pyrrole and (b) its monolayer polymerization product on KBr	79
2-21	^{13}C -NMR spectrum of Langmuir monolayer polymerized 3-benzodicyl pyrrole and the suggested chemical structure	80
2-22	CPC data of different composition of SHEP and HQEP	83
3-1	Structure of MALDI matrix used in this study	87
3-2	ESI spectrum of DTL mixture	94
3-3	MALDI Spectrum of HQEP	95
3-4	MALDI Spectrum of SHEP	97
3-5	MALDI-TOF spectra of 50% SHEP and HQEP copolymer with matrix DTL in $\text{CH}_2\text{CN}/\text{THF}/\text{EtOH}/\text{AcOH}$	98
3-6	MALDI-TOF spectra of SHEP homopolymer with matrix DTL in $\text{CH}_2\text{CN}/\text{THF}/\text{EtOH}/\text{AcOH}$	100

3-7	Daughter species evolution after CID	39
3-8	Fragmentation of monomers	100
3-9	Fragmentation of partially oxidized HEDP monomer	100
3-10	Fragmentation of the dimer of HEDP	101
3-11	Mass spectrum of polyHEDP with ESI/APCI-QIT techniques	101
4-1	Flexant AXS Flatflex TM instrument and a schematic of radiation gun of the sample	108
4-2	Schematic of the Reflection Geometry	109
4-3	Sketch of monolayer trough cell	109
4-4	Schematic diagram of monolayer trough cell for X-ray diffraction experiment	110
4-5	Synchrotron X-ray diffraction setup	111
4-6	Schematic of the Synchrotron X-ray Diffraction setup	113
4-7	Powerder diffraction pattern of HEDP	117
4-8	Powerder diffraction pattern of MOEP	118
4-9	Diffraction image of 12 multi-layer HEDP L3 film	119
4-10	The two monomers in their staggered conformation and their calculated lengths	121
4-11	Diffraction of Langmuir-Blodgett monolayer film	123
4-12	Contour plots of the Synchrotron X-ray diffraction from the Langmuir monolayers at 21 °C of the polymers	125
4-13	Contour plots of the Synchrotron X-ray diffraction from the Langmuir monolayers at 21 °C of the monomers	126
4-14	The periodicity of the condensed hexagonal model	127
4-15	The periodicity of the distorted hexagonal model	127
5-1	Schematic of HEDCAT formation	130

3-2	Schematic of the experimental setup (3DID-1) at MRCAT beamline.....	130
3-3	Beam profile in the X_y direction, at $X_{gap}=0$ with poor beam-optics.....	130
3-4	Beam profile in the X_y direction, at $X_{gap}=0$ with improved beam-optics.....	130
3-5	The trough setup at the MRCAT beamline.....	131
3-6	The symmetric barrier driven of the Langmuir trough.....	134
3-7	The rectangular-trough with the sealant.....	134
3-8	Schematic of the new trough setup.....	137
3-9	Two different shapes of troughs.....	141
3-10	The second trough that would replace the first for cleaning purpose.....	142
3-11	Schematic of positions of beam detectors.....	145
3-12	Special optical table built for the 3DID setup.....	147
3-13	Diffraction pattern of the standard (C20 steel) Mn/Ni.....	148
3-14	Diffraction pattern of the standard (C20 steel) at 5°C and Mn/Ni.....	150
3-15	Contour plots of the Synchrotron X-ray diffraction from the Langmuir monolayers at 15°C of the amonons.....	151
3-16	Contour plot of the Synchrotron X-ray diffraction from the Langmuir monolayers at 15°C of the MPPs H2OP.....	152

*Abstract of Dissertation Presented to the Graduate School
of the University of Florida in Partial Fulfillment of the
Requirements for the Degree of Doctor of Philosophy*

**STRUCTURAL INVESTIGATION OF COPOLYMERIZATION REACTIONS IN
RESTRICTED DIMENSIONS**

By

Gajanya Wamanthani

May 2009

Chairman: Professor Randolph S. Stein
Major Department: Chemistry

When polymerized by conventional methods, active sites could attack in any direction. In Langmuir monolayers, not only has the reaction medium reduced from three dimensions to two, but also the monomer molecules are oriented in a specific way with respect to the air-water interface, under pressure. This specific orientation of the monomers should alter the reactivity compared to the solution polymerization. In this study we attempted to find differences in a series of copolymers synthesized via Langmuir monolayer technique versus conventional synthesis procedures by analyzing their molecular weight distribution, sequencing distribution, and the lateral order when spread on the air-water interface.

Monomer mixtures of 3-bromobenzyl pyridine (MBP) and 3-methylbenzyl pyridine (MBMP) were polymerized in monolayers at aqueous surfaces, then transferred to hydrophobized silica substrates. While some of the components of their polymers could be

transferred to hydrophobic substrates using Langmuir-Blodgett techniques, monomer monolayers could be transferred successfully to hydrophilic surfaces from where subsequent clipping apparently resulted in Y-type multilayers. Experiments suggest that 40% and 60% monomers of both MDP and NMDP pack better on the surface interface than MDP alone.

Molar mass and initial copolymerization rates were gauged by matrix-assisted laser desorption/ionization time-of-flight mass spectrometry (MALDI-TOFMS). Further investigations of the polymer were done using ion trap mass spectrometry.

Lateral ordering was investigated by X-ray diffraction, largely at synchrotron sources and including the Materials Research Collaborative Access Team (MRCAT) beamline at the Advanced Photon Source (APS) in Chicago, Illinois. A custom-made grazing-angle X-ray scatter diffractometer was commissioned at Sector 10 (MRCAT) of the APS synchrotron at Argonne National Laboratory (ANL), the construction and commissioning was the main focus in the final year of this dissertation work. The primary goal was to collect data much faster (at this 7 GeV synchrotron source) than possible at National Synchrotron Light Source in order to observe structural evolution in real time during polymerization reactions. Several different X-ray detectors were tested to optimize the total experimental time. Curved and linear position sensitive detectors, as well as conventional scintillation detectors with appropriate buffer slits, were tested. Double mirror X-ray beam steering optics and a custom designed Langmuir trough system have been built and installed for all users of the beamline.

CHAPTER 1 INTRODUCTION

1.1 Langmuir and Langmuir-Blodgett Films

Polyaniline and polypyrrole have been the focus of great attention due to their anisotropy and high electrical conductivity.^{1,2,3} These otherwise poorly soluble polymers can be made soluble in common organic solvents in a covalent state or as a low molecular mass through functionalization with appropriate side groups,⁴ or counterions.^{5,6} Furthermore, highly oriented thin films of these functionalized polymers can be made by the Langmuir-Blodgett (LB) technique.⁷ Preliminary work on these thin films has shown interesting anisotropic optical and electrical properties.^{8,9} Such films may prove to be useful in understanding low-dimensional conductors. Polyaniline and polypyrrole have been polymerized successfully into three films and built into multiple layers by LB methods.^{10,11} However, the resulting films always have a substantial number of defects due to overlapping chains, which results in a low well-defined two-dimensional (2-D) nature.

One method of forming a film with a better defined 2-D structure is by polymerizing a pre-formed highly oriented monolayer of monomer. Under these polymerization conditions, it is likely that a polymer monolayer resulting from a self-avoiding walk in two dimensions occurs. To date, there exists no simple experimental technique to directly verify such a monolayer. However, knowing Tumbling

Microscopy (STM) measurements have indicated²⁰ that monolayers polymerized from which are transformations which substrates do not contain overlapping chains. Monolayers of some 3-alkyl pyridine on a Langmuir-Blodgett have been polymerized in this way.²¹⁻²³ With more recent exceptions,^{21,22} 3-alkyl pyridine have only been polymerized on the LB trough when a large amount of substituted pyridine was present. The resulting polymer was largely nonconjugated polypyridine from excess pyridine monomer diffusing to the surface from the solution.^{24,25} The resulting thin films had very interesting properties (such as conductivity) but were not monolayers in the conventional sense.

In this thesis we have shown that 3-alkyl pyridine²⁷ and a mixture of 3-alkyl pyridine and 2i-alkyl pyridine can be polymerized using the Langmuir method. Polymer obtained from this method has been characterized using conventional analytical techniques. Also, grazing incidence X-ray diffraction (GIXD) of these monolayers was obtained to investigate structural organization of these monolayers at air/water interface. The theme of the GIXD experiment was very important since we designed, built, and obtained data from an apparatus at the Synchrotron at Argonne National Laboratories. The rest of this chapter provides a brief history and some basic knowledge of the techniques employed.

1.1.1 History of Langmuir and Langmuir-Blodgett Films

The first important experiment in monolayers was reported when Dr. Benjamin Franklin presented a well-documented²⁸ scientific experiment at the Royal Society in 1774, claiming that a drop of oil spread over an area of water that half its size.

produced as oil film only monolayers thick. About a century later, first, Lord Rayleigh²⁴ and then Agner Poulson²⁵ proposed that oil spread on a water surface is only one molecule thick, but Dr Irvin Langmuir was the first person to fully appreciate and develop a theory for monolayers.^{26,27,28} To acknowledge his numerous contributions to the field, monomolecular films of organic materials at air-water interface were named as Langmuir films. Dr Irvin Langmuir was awarded the Nobel Prize in chemistry in 1932. He was the first to describe the expansion of monolayers at the air-water interface and the two-dimensional phase transitions of the monolayers. Katherine Blodgett joined Langmuir's research at General Electric in 1919. Langmuir and his co-worker, Blodgett, applied this technique extensively and showed that fully wet monolayers can be transferred successfully to a solid substrate layer by layer to build multilayers.^{29,30} Building up monolayer assemblies are now known as Langmuir-Blodgett (LB) films.

Interest in the field of monolayers expanded, and as a result many books were published by authors such as Eric Nielsen,³¹ Neil Adams,³² William Harkins,³³ and Arthur Adamson.³⁴ George Gomer's book, *Interfacial Monolayers at the Liquid-Gas Interface*,³⁵ has thoughtful discussions and is a standard reference for all new students in the field. The authors, A. Ulman,³⁶ G. Roberts,³⁷ and M. Petty³⁸ have published relatively newer books on the subject of monolayers and LB films. Interest in LB films has grown significantly since the 1970s because of the work of Hans Kuhn³⁹ and his colleagues on energy transfer in multilayer systems. However, poor film quality, irreproducible results, and lack of new materials kept work on LB films moving at a slow pace. There were some early developments in Langmuir films in the 1930s,^{29,30} but relatively little was done until recently, when research into LB films became more demanding.⁴⁰ In recent years, LB

These have received much attention from the scientific community, especially with the new materials being synthesized every day. Some of the most notable scientists in the monolayer field include Randy Datta, Polak Datta, Francis Gantier, Jerome Lachet, Hazen McConnell, Egoner Möller, Holger Möller, Holger Ringdorf, Michael Rübner, and Gerhard Wegner. In order to get a better understanding of these monolayers, basic physical properties of monolayers are described below.

3.1.1. Basic Concepts of Langmuir Monolayers

There are different interfaces (such as solid/sol, solid/liquid, etc.), but only the air/liquid (air/water) interface will be discussed in this work. Due to differences in the environments, the surface of the liquid always has excess energy, which is called surface tension (γ). It is described thermodynamically as

$$\gamma = (\partial G / \partial a)_{T,P,n_i} \quad (3.1)$$

where G is the Gibbs free energy of the system, a is surface area, T is temperature, P is the pressure, and n_i is the composition. T , P , and n_i are held constant. Water at 20°C has a surface tension of 72 mN/m.

Typical monolayer-forming materials contain two characteristic features in the molecule. One part is a hydrophilic head group, and the other is a hydrophobic tail (normally a long alkyl chain). These types of molecules are called surfactants or surface-active agents. When a solution (such as a dilute solution) of these surfactants is spread over the air/water interface, the solvent evaporates to leave behind the surfactants on the water surface. Due to the amphiphilic nature of these molecules, the head groups are immersed in the water while the tail groups remain on the surface. Since a very small concentration

of molecules is spread on the surface, the interactions between molecules is reduced, and the resulting phase is termed a two-dimensional gas. The water surface tension is minimally affected in the gaseous state (Figures 1-1), but when the molecules are forced to restrict the available area, the surfactant molecules exert a repulsive force against one another. A two-dimensional analog of pressure is created, which is termed surface pressure. When the surface pressure (Π) is at equilibrium, the following relationship holds:

$$\Pi = \gamma - \gamma_0 \quad (1-2)$$

where γ is the surface tension of the pure water surface and γ_0 is the surface tension at the interface where the monolayer is present. The first sharp increase in the surface pressure is known as the onset of the monolayer. The maximum Π that can be observed at the air/water interface at 30°C is 110mN/m (when $\gamma_0 = 0$). Since the dilated interface area and the number of molecules spread on the interface are known, the mean molecular area (A) could be calculated for each known position. The mean molecular area is the widely used parameter in this test, such as surfactant monolayers, the A is a function of A .

Even though both a Langmuir-Blodgett²² and a Wilhelmy method²³ balance were available, only the Wilhelmy method balance was used in the experiments discussed in this text. The sensitivity limit of this technique was 0.001mN/m. When the test plate is completely wetted by the liquid, the downward force (F) was measured as indicated in Figure 1-1 and given by the following relationship:

$$F = \rho_L g h a + \gamma_0 (1 + \alpha) \cos \theta - \rho_s g a h \quad (1-3)$$

where γ is the surface tension, θ is the contact angle of the liquid on the solid plate, ρ_L

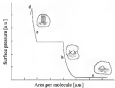
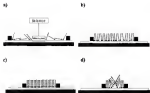


Figure 5-1 Surface pressure versus area per molecule isotherm for a long chain organic compound and the corresponding molecular arrangement at the surface (Giacca). **a)** Liquid-expanded; **b)** Liquid-condensed; **c)** Collapsed.

and ρ are the densities of the plate and the liquid, respectively, and g is the gravitational constant. The plate dimensions are defined as length (l), width (w), and thickness (h) of the plate, and the plate is submerged in the liquid to depth h . The thickness (h) of the plate is negligible compared to the width (w), and when the plate is completely wet ($\cos\theta = 1$), the force (F) is constant. Therefore the following relationship holds:

$$F = -\frac{\rho}{2} \rho_L g w h \quad (1-40)$$

a)



b)



Figure 1-2 Diagram (a) is a top view showing forces acting on the Wilhelmy plate. a) Top view, b) Side view

Another important property of Langmuir films is the surface potential, ΔV . This property expresses the change in the phase boundary potential produced by the addition of an interfacial film. A monolayer film at the air/water interface can be treated as an

assembly of molecular dipoles that can shift the potential across an interface. The $\Delta\psi$ can be related to an apparent or surface dipole moment, μ_a , using the Helmholtz equation,

$$\Delta\psi = \mu_a N / \epsilon_0 \quad (1-3)$$

where ϵ_0 is the permittivity of a vacuum, N is the concentration of dipoles at the interface, and μ_a is the dipole moment normal to the interface. The value of μ_a is affected by the orientation of the surfactant molecules at the water/air interface. The dipole moment is made up of three components: μ_w , the moment of the water molecules at the interface, μ_{gr} , the dipole moment from the head group, μ_{lg} , the dipole moment from the hydrophobic group. μ_a is defined by the following equation,

$$\mu_a = \left(\frac{P_1}{\epsilon_1} + \frac{P_2}{\epsilon_2} + \frac{P_3}{\epsilon_3} \right) \quad (1-4)$$

where ϵ_1 , ϵ_2 , and ϵ_3 are the local dielectric constants of each of the three layers.

A popular method by which the surface potential of a Langmuir film can be determined is by the vibrating plate method, which will be described in the section 2.2.1.4.

The apparatus available in our lab to investigate Langmuir films is described in Section 2.2.1.1. There are many companies, such as KSV, Joyce-Loebl, Cantal, and Loeb, which manufacture such apparatus. These companies provide complete interfacial characterization instruments, all based on the same fundamental principles. The whole system can be coupled with different spectroscopy techniques, including Brewster angle microscopy (Section 2.2.1.3),³⁰ fluorescence microscopy,³¹ light reflectors,³² UV-Vis,³³ and FTIR.³⁴ The ability to transfer these Langmuir monolayers to

solid substrate is very important, and a brief discussion of Langmuir-Blodgett film (transfered film) is done in the following section.

1.1.3 Monolayer Film Deposition on to a Solid Substrate

Langmuir-Blodgett film deposition on a solid substrate is explained in Section 1.2.1.3. The transfer of Langmuir film can take in the "liquid-expanded" or in the "liquid-condensed" state because the film is less rigid in these thermodynamic states.

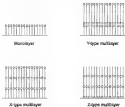


Figure 1-5. Deposition types of LB films.

When the monolayer is held with surface pressure, a dipping device moves the substrate up and down through the surface of the water, which transfers the monolayer to a solid substrate. Surface pressure, dipping speed, nature of the substrate, and characteristics of

The monolayer, one more of the parameters that have to be adjusted in order to obtain a proper transferred film. The monolayers change transferred at a surface pressure between the on set and the collapse pressure. The quality of the transferred film was measured using a parameter called the transfer ratio (ξ), which has the following relationship:

$$\xi = \frac{A_1 - A_2}{A_1} \quad (1.3)$$

where A_1 and A_2 are the initial and final surface areas of the monolayer, and A_1 is the surface area of the solid substrate.

The nature of the substrate and the monolayer influence the interactions between them. By varying starting position of the transfer of the monolayer, one could obtain different types of LB films (Figure 1-3). Figure 1-4 demonstrates how Y-type LB film was obtained using a hydrophilic surface substrate and apolar as the first movement of the substrate. Cleaning and modifying of the substrate surfaces are explained in Section 2.1.3. The Y-type films were the most common and could be obtained using a hydrophilic or a hydrophobic substrate surface. The X-type films can be obtained utilizing Schaefer's method,⁴⁷ but Z-type films are rare. Recent investigations (analysis of Langmuir and LB films have shown that rearrangement of the monolayer takes place before after deposition.⁴⁸ If the processes of drying and annealing were carefully controlled, one may be able to manipulate the LB phases to achieve or influence their structure such that they contain fewer defects, preferably domain size, and domain orientation.

By using multi-component troughs, one could transfer various types of monolayers with different characteristics. These multi-component LB films are very

radial hole in biological research and in building structures (driven rock core) properties.

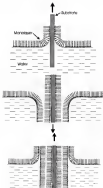


Figure 1-4 Tensioning on Y-type LIFT wellbore in a hydrocarbon reservoir.

1.1.4. Polymerization at the Air/Water Interface

Transfered LB-films of low molecular weight surfactants have had relatively little use as potential new applications⁴⁸ because of their solubility, thermal instability, and molecular rearrangement. These problems cause the desired electrical and/or optical properties of the potential devices to be lost or reduced. One solution for overcoming the problems of low molecular weight surfactants is to use pre-formed polymers with amphiphilic character, but there is controversy as to whether or not pre-formed polymers Langmuir films under pressure are true monolayers. Another disadvantage is the difficulty of transferring due to the rigidity of the polymer, although it has been suggested that this problem can be overcome.⁴⁹

Another solution is to transfer the monomer onto a solid substrate that will then induce photochemical polymerization (usually UV- or visible-light).^{50,51} The major concern with this method is the rearrangement of molecules upon polymerization, which gives large defects. A third solution is first to form the monolayer on the surface under pressure and then to polymerize the material while maintaining constant surface pressure. This method forces the monomer surfactants to remain oriented while polymerization is taking place. The third method results in monolayers which show enhanced mechanical and physical properties.⁵² These enhanced mechanical and physical properties provide improved electronic properties for new devices constructed with the new polymeric material.

Recent research has gone to great lengths in order to compare two-dimensional polymerization to well known methods of three-dimensional polymerization. These

comparisons provide a better understanding and control of two-dimensional systems.^{20,21}

MacIntyre's *Chemistry of Surfaces*²² has a good review of this subject.

The general expression for a monolayer with first-order kinetics is given by the following equation, which applies to a surface reaction at constant interfacial pressure.

$$x = a_0 \exp(-kt) \quad (1.11)$$

$$\frac{(A - A_\infty)}{(A_0 - A_\infty)} = \exp(-kt) \quad (1.12)$$

The initial concentration of monolayer is given by a_0 , x is the concentration at time t , k is the first-order rate constant, A_0 is the initial area of the monolayer, A_∞ is the area after the completion of the reaction, and A is the area at time t . Other monolayer properties such as surface potential or viscosity with respect to polymerization rate could be monitored, but these will not be discussed in this text.

One comparison to most of the monolayer properties discussed here is that monolayer π is thermodynamically equilibrium. Additional information about the thermodynamic aspect of monolayers is discussed in the following section.

The proposed mechanism for the random polymerization of pyridine is shown in Figure 1-5. The first step is oxidation of pyridine to yield a radical cation. The second step is a randomization step and there are two suggestions. The coupling process can be proved by the recombination of two radical cations to yield a dimeric pyridine dication (3a) or electrophilic addition of the pyridine radical cation to pyridine to form by-products to a dimeric pyridine dication. The third step is elimination of two protons to regenerate the system. Further coupling with monomeric radical cations would produce a trimer, etc.

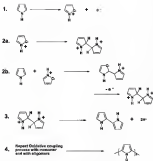


Figure 1-4— General mechanism for the oxidative polymerization of phenols

1.2 Thermodynamics of the Langmuir Monolayers

The two-dimensional monolayer isotherm (Π versus A) serves as analog for the much familiar p versus V isotherm for ideal gases. The gaseous state, liquid-expanded state, and liquid-condensed state in two-dimensional phases are analogous to gaseous state, liquid state, and solid state in three-dimensional phases. The concept of analogy in these two different worlds was first suggested at the beginning of the century¹⁸. The change in the slope of the isotherm reflects a transition point similar to phase transitions in three-dimensions. The two very distinguishable phase transitions that any amphiphilic molecule shows at the interface are co-set and collapse. The co-set is the first transition that takes place when surfactant molecules reach the liquid-expanded state from gaseous. The second phase transition from the liquid-expanded is the liquid-condensed phase, which is indicated by a slight increase in the slope of the isotherm. When the monolayer cannot withstand the surface pressure and breakdown, it forms bilayers and multilayers, which is termed collapse. However, the collapse transition is generally thermodynamically irreversible and has a large hysteresis.

1.2.1 Two-dimensional Equation of State

Just as in the three-dimensional world, when the monolayer molecules have sufficient distance between them, they must vary little from one another. This is called the gaseous state. Thermal motions cause the expansion, and a "two-dimensional vapor pressure" exists in this state. By applying the ideal gas law, the following relationship is obtained:

$$\prod_{i=1}^n A_{i,trans} = kT \quad (3-10)$$

For this expression, k is the Boltzmann constant, and it is assumed that surfactant molecules are moving with an average translational kinetic energy of $\frac{1}{2}kT$ for each degree of freedom. Since the surfactant molecules have interactions with the liquid molecules of the sulphate, this system is considered to be an extremely dilute insoluble layer in contact equilibrium. In contact equilibrium, the monolayer is forced to remain on the surface, and the water molecules are in equilibrium beneath the surface.⁽²⁾ Since the amphiphilic molecules take some surface area, the above ideal gas was changed to

$$\prod_{i=1}^n A_{i,trans} = A_s kT \quad (3-11)$$

where A_s is the area corresponding to the osmotic value. Various other expressions have proposed to explain the negative deviation from the ideal value of the ΠA product, but these expressions are not discussed here.

3.3.2 Monolayer Phase Transitions

The most common first order transition is at the onset of an isotherm, where the gaseous state reaches the liquid-expanded state. Upon further compression, some monolayer isotherms exhibit an increase in the slope, which can be attributed to the reaching of the liquid-condensed state. The slope of an isotherm is related to the compressibility (C) as follows:

$$C = - \left(\frac{1}{A} \right) \left(\frac{\partial A}{\partial \Pi} \right) \quad (3-12)$$

where C has been calculated at a particular point in the isotherm. The compressibility describes the competition of the lateral packing and the elasticity of the monolayer

Many other phase transitions have been discovered by investigation of the lateral packing of the monolayers utilizing synchronous X-ray diffraction.¹⁸ Most of the monolayer investigations (simple long chain alcohols) have shown that the lateral packing is hexagonal or distorted hexagonal. By employing this technique, the tilt angle of the molecules can be measured, whether the tilt is around the nearest neighbor or between neighbors. Most importantly, with X-ray diffraction, the phase transitions can be seen more accurately and in much greater detail.

3.3.1 Mixed Monolayers

Mixed monolayers can be obtained when two or more surfactants are spread onto the aqueous interface. Such monolayers can be miscible, partially miscible, or phase-separated, depending on the physical properties of the surfactants and the nature of the solvent. The miscibility can be investigated by studying some thermodynamic properties (such as surface tension, surface phase rule, and free energy of mixing) of the mixed monolayer as a function of the composition. The simple and quick way is that the miscibility of the mixed monolayers is to see whether the isotherm contains the individual collapsed pressure of each component, which represents separate monolayers, or if it has a single collapse pressure which indicates miscibility. An immiscible monolayer behaves like two different monolayers at the interface. If the distance are small enough, then the average surface property, $\bar{\chi}_{LM}$ (such as mean molecular area, surface potential, compressibility, etc.), can be obtained from equations 1-13:

$$\bar{\chi}_{LM} = R_1\chi_1 + R_2\chi_2 \quad (1-13)$$

\bar{X}_i denotes the molarlike value of a property of the binary mixture, N_1 and N_2 are the mole fractions, and \bar{X}_1 and \bar{X}_2 are the measured values for the pure films.

Another important thermodynamic property of the mixed monolayers at low energy of mixing, ΔG_{mix}^0 , which was described by Goodrich.¹² For ideal mixing of a two-component system,

$$\Delta G_{\text{mix}}^0 = RT[\bar{X}_1 \ln \bar{X}_1 + \bar{X}_2 \ln \bar{X}_2] \quad (1-14)$$

when $\Pi \rightarrow 0$. The excess free energy of mixing (ΔG_{mix}^E) can be calculated for a binary mixed monolayer at any finite surface pressure (13). The ΔG_{mix}^E was determined by the free energy for an ideal mixed film (calculated from the pure films) and by the binary mixture isotherms according to the following relationship:

$$\Delta G_{\text{mix}}^E = \int_0^\Pi A_{\text{mix}} - (N_1 A_1 + N_2 A_2) d\Pi \quad (1-15)$$

where A is the surface area and N is the molar fraction of the regions considered.

Deviations from the ideal situation (equation 1-14) indicate nonideality and non-ideality of molecular interactions. Although such deviations (mainly negative deviations) are seen in many multi-component systems, the interpretations of their significance have been speculative. The largest effects were observed when one component formed a [liquid]-condensed state, and the other component formed a [liquid]-expanded state. Goodrich found that the free energies of mixing were similar regardless of the chemical nature of the polar group and suggested that chain-chain interactions were more important in these mixed monolayer systems. Interpretation of these deviations from the ideal is very difficult while only using the Π - A measurements. Other characteristics of mixed monolayers (such as surface potential, surface viscosity, and evaporation rate) are needed

to better understand the molecular interactions. In this text, reliability of the stated monomers will be supported using the ^{31}P measurements and surface potential data.

1.3 Mass Spectrometry

During the past few years, there has been increasing interest in the application of mass spectrometry for characterizing synthetic polymers. The main advantages of mass spectrometry are the speed of analysis, the ability to measure absolute mass values, and the ability to obtain the relative molecular weight distributions. Unlike mass spectrometry, the conventional polymer characterization techniques (gel permeation chromatography (GPC)²⁶, light scattering, NMR spectrometry²⁷, osmometry, cryology etc.) normally provide bulk sample information.

Rapid advances in the field of polymer chemistry have produced an increasing number of new polymers that are widely different in composition and chemistry. In addition to the molecular weight, the physical properties of these polymers are dependent on the monomer composition, monomer sequence, and type (block, graft, linear, etc.) of the polymer²⁸. It is very important to determine the overall chemical composition and structure in order to determine the property relationships, the mechanism of the polymerization, and the effects of reaction conditions on the polymer structure.²⁹

Mass spectrometry requires gas phase ions. The low volatility of macromolecules has served to limit this application. Recent advances in matrix-assisted laser desorption/ionization (MALDI)³⁰ and electrospray ionization (ESI)³¹ have emerged as suitable techniques for the characterization of synthetic polymers because these

techniques^{38,39} have been able to provide the distribution of polymers without fragmentation.

3.3.1. Overview of MALDI

Since the 1970s, laser desorption has been used in mass spectrometry, but it often produces fragment molecules. Matrix-assisted laser desorption/ionization (MALDI), which can desorb and ionize thermally labile and aromatic macromolecules, was introduced in 1988 by Karas et al.⁴⁰ and by Hillenkamp et al.⁴¹ This technique was developed for and first applied to biopolymers. MALDI/TOFMS is ideally suited for synthetic polymer analysis because of the simplicity of the mass spectra which show mainly singly charged molecular ions with very little fragmentation. TOF analysis in which very high molecular weight polymers can be analysed (over 10^6 Da),⁴² and state-of-the-art reflection instruments equipped with delayed ion extraction ion sources.^{43,44} Recently, there has been a growing interest in MALDI/TOFMS analysis of synthetic polymers.⁴⁵⁻⁴⁸

The matrix used for MALDI often serves a dual role. It absorbs energy from the pulsed laser beam, ionizes the sample molecules, and carries the sample molecules via molecular collisions.⁴⁹ Although the details of the energy conversion,⁵⁰ proton affinities of matrices,^{51,52} sample desorption, and ionization continue to be studied, a general description of the mechanism is as follows.⁵³ Energy from the laser beam is absorbed by the chromophoric matrix, which rapidly expends into the gas phase surrounding the analyte molecules. Ionization occurs by proton transfer between excited matrix molecules and analyte molecules. Ionization is aided by collisions, which occur in

the expanding plasma ions are stored into the mass analyzer, which measures the mass-to-charge ratio (m/z), usually plotted against ion abundance.

Experimental variables in MALDI will include the matrix and the ratio of matrix to analyte concentrations, laser intensity, wavelength and pulse-width, and the choice of negative ions or positive ions. Nitrogen lasers with wavelengths in the ultraviolet (UV) range (337 nm) are the most commonly available laser source for commercial MALDI mass spectrometers. The laser is pulsed so as not to pyrolyse the sample. UV-absorbing aromatic compounds are most commonly used as matrices,¹⁸ and various aromatic acids and alcohols provide excellent sensitivity for forming protonated ions.

Many types of mass spectrometers are used with MALDI, including time-of-flight (TOF), Fourier transform (FT), magnetic sector, sector-TOF, ion trap-TOF, and TOF-TOF instruments. Of these instruments, FT analyzers give the highest resolution of ions described by MALDI, and this combination is becoming increasingly popular. However, currently the TOF analyzers are most commonly used with MALDI. Ion analyzers such as the TOF and FT can be synchronized with the computer produced by the laser. This triggering delay increases the sensitivity of the instrument, which is currently in the attomole to femtomole range. TOF instruments have an unlimited mass range, and they are rugged, simple to operate and relatively inexpensive. Actually, MALDI provided the boost to develop TOF mass spectrometers.¹⁹ The mass accuracy of MALDI-TOF instruments is generally 3–5 000 ppm, and resolution can exceed 1 part in 20,000.

1.5.4 Overview of ESI

Electrospray ionization (ESI) was first developed to analyze a polystyrene solution by DeLaet *et al.*²¹ in 1981. However, this technique did not gain popularity until the 1980s when Fenn and coworkers²² used ESI to analyze biocatalytic in polar solvents. In 1988, Fenn and coworkers demonstrated the capability of ESI to desorb synthetic polymers,²³ and later work extended the detectable molecular weight range to 5 million.²⁴ Liquid chromatography (LC) techniques in polymer analysis are quantitatively reliable. State-of-the-art LC of synthetic polymers recognizes different modes of separation. Size-exclusion chromatography²⁵ (SEC) or GPC separates the polymer according to the hydrodynamic volume of the eluent, directly related interaction with the stationary phase, and is the established method for the determination of the molecular weight distributions of the polymer.

Typically for ESI, the analyte is dissolved in a solvent (10^{-3} M) and introduced through a capillary at a flow rate of 2–5 μ L per minute. There is a constant flow of bath gas (e.g., N_2) surrounding the end of the capillary to desolvate the solvent. High voltage is applied between the end of the capillary and the heated capillary at the mass spectrometer entrance in order to break the solvent into droplets and focus the analyte. In ESI-MS, experimental parameters such as the solvent employed, the temperature and flow velocity of the bath gas, the potential drop at the end of the capillary, and the distance between the capillary and the orifice cone influence the success of the ESI-MS experiment. Electrospray ionization can be used with a wide variety of mass analyzers but is most frequently used with an ion trap, quadrupole, and Fourier transform ion cyclotron resonance mass spectrometers.

1.3.3 Operation of APCI

Early developments in atmospheric pressure ionisation (API) sources by Hines and co-workers^{28,29} have led to modern atmospheric pressure chemical ionisation (APCI) sources³⁰ for LC/MS coupling. In the original API setup, 1-2 μ L of a liquid sample was injected through a syringe to a atmospheric pressure nebulisation chamber. A hot carrier gas (N_2) was introduced into the chamber to help nebulisation and to transport the analyte as an aerosol to a subsequent β -source (^{90}Ni). The gas molecules were ionised in that area, producing an atmospheric pressure reagent plasma that gave rise to analyte ions through ion molecule reactions. Ions were then transferred to the mass analyser through a very small opening.

The widespread success of ESI technique in HPLC's resulted in optimized API sources for LC/MS coupling. The modern APCI interfaces use a heated pneumatic nebulizer probe for nebulization and a high voltage needle to produce a corona discharge which causes solvent ionization. The sampling orifice can be a sampling cone or a heated capillary made of glass or stainless steel and the probe can be situated axial or orthogonal to the sampling orifice.

APCI is currently applied to analysis of a variety of compounds, mostly in the environmental³¹ and pharmaceutical fields.³² This technique is not as effective as ESI for the analysis of lipopolymers.³³ However, APCI is very effective in the analysis of medium and low-polarity compounds³⁴ or when relatively non-polar solvents have to be used. This technique was used in this dissertation work to analyze the monomers and the polymeric materials obtained by the Langmuir method.

1.3.4. Current Usage of MALDI, ESI, and APCI in Polymer

Both MALDI and ESI have been popular among polymer chemists because of the soft ionization that occurs with these techniques. When a new polymer is synthesized, it is very important to know the molecular weight distribution and the average molecular weights (such as \overline{M}_n , \overline{M}_w , and \overline{M}_z) since these characteristics are directly related to the physical properties of the polymer. Using ESI and MALDI, these useful parameters can be obtained in a short time (e.g., 15 min.) from a small amount of polymer material (less than 1 mg). Molecular weight data often yields information about details of the polymer structure (e.g., sequence of repeat unit, end groups) and information about the impurities, which are present in the sample.

Most reports of the developments of MALDI for polymer characterization have been concentrated on poly(ethylene glycol)²² (PEG), poly(methyl methacrylate)²³ (PMMA), and polystyrene²⁴⁻²⁷ (PS) and the information obtained has included both the molecular weight distributions and the identification of end groups. These three polymers have been studied with a variety of matrices in order to find an optimum matrix for synthetic polymers. Since each polymer has unique characteristics, the identification of one ideal matrix has been unsuccessful, but several adequate ones have been found. Also, the addition of cations (Na^+ , K^+ , Ag^+ , etc.) has helped to enhance the MALDI signal, and the effect of various cation attachments to the polymer has been studied.^{28,29}

In MALDI, singly-charged ions are preferentially produced. When MALDI is coupled with TOF, the mass range of the polymer sample is quickly obtained. Some groups have taken advantage of this technique to study statistical

copolymerization.^{36,37,38} After obtaining the mass spectrum, each peak is assigned to a unique molecular species based on the mass-to-charge ratio. In order to assign these peaks, a high-resolution mass analyzer, which can be achieved by the use of a reflection TOF mass spectrometer, is required. Since the mass spectrum is representative of the copolymer present, it contains a record of all the reactions that occurred in the polymerization. By relating the composition and the kinetics to the probabilities associated with each possible reaction mechanism in polymerization, it should be possible to estimate some kinetic parameters. Theoretical statistical interpretations of this class of problems are well-developed,^{39,40} so the theoretical values can be compared with the results obtained from mass spectrometry.

Electrospray ionization, unlike MALDI, produces multiply-charged ions. Multiply-charged ions are sometimes considered a nuisance because of overlapping peaks, but there is an advantage to reducing the m/z values. Since the mass analyzer measures the m/z, much higher molecular weight ions can be measured if they have a higher charged state. However, unlike MALDI, the use of electrospray ionization to characterize synthetic polymers has been limited.

An advantage of ESI is the compatibility with liquid chromatographic methods such as Size Exclusion Chromatography (SEC) and High Performance Liquid Chromatography (HPLC). Electrospray mass spectrometry without chromatographic separation is adequate for the characterization of synthetic polymers in terms of the determination of molecular mass, end groups, and molecular weight distributions. However, the molecular weight distribution is difficult to obtain when the distribution is broad. By coupling SEC with ESI, much better results have been obtained⁴¹ than with

electronic EDS-ME.³⁰ Relatively higher voltage concentrations have been needed for the examination of less polar polymer samples.

1.4. X-ray Diffraction

Wilhelm Conrad Röntgen first discovered X-rays in Würzburg, Germany, on November 8, 1895. Six months later, X-rays were used on the battlefield to photograph bones inside the body. In 1901, six years after his discovery, he was awarded the Nobel Prize, the first time one was awarded for the field of physics. The first X-rays were produced using gas-filled cathode-ray tubes, but a century later vacuum-sealed tubes, rotating anodes, and synchrotron sources are utilized for experimental and medical work. The general effect of X-rays on living cells is a lethal one, but this is the basis of their therapeutic applications. Early workers using and studying X-rays suffered from dermatitis and other diseases because they were not aware of the chemical and biological effects of X-rays.

A variety of applications in the field of X-rays is widely used. Radiography is the oldest application for X-rays and is still in use today. The much familiar security check on luggage is a common application for X-rays. The first use of X-rays for structural investigation of materials (X-ray diffraction) was done by Max von Laue in 1912. The father-son team of William Henry and William Lawrence Bragg introduced the simple Bragg Law, $n\lambda = 2d \sin \theta$, which is widely used even today. Of relevance is that demonstrates, when a layered system diffracts there should be a series of peaks. Arthur Compton first observed the total scattered reflections of X-rays at the University of Chicago in the early 1920s. Techniques in electron probe X-ray microanalysis were

developed mainly in Great Britain in the 1950s. This is a very powerful method of microanalysis of surfaces for the determination of composition and for chemical phase mapping.

Even though synchronous radiation was first observed as early as 1945, the first source to be dedicated for X-ray production was not built and opened until the early 1980s. This and several which followed it are considered "first generation" sources. Indeed, X-ray generation at such sources was "passive" in which energy particles (electrons) excite transitions. Current sources are "third generation" sources (Table 1-1). Such sources are specifically designed for the production of X-rays and also are designed to incorporate insertion devices, undulators and wigglers, which produce very high brightness, monochromatic, collimated beams. Brightness, a measure (Figure 1-4) of mean or characteristic beam intensity, of several different X-ray sources is shown in the Figure 1-4. The line of the radiation does not reflect the advantages of synchronous X-rays. The brightness, brilliance, of the X-ray beam is defined in terms of the number of photons $s^{-1}mm^2$ for a given energy bandwidth. Also the radiation emitted is elliptically polarized in the plane of the electron orbit. The availability of the very high intensity continuous spectrum of synchronous radiation source has provided the opportunity to perform research which was impossible by other means. For instance, the technique of X-ray absorption spectroscopy (EXAFS and related techniques) has been enabled by such synchronous. Also, Protein crystallography is moving from university laboratory instruments to synchronous, and grazing incidence diffraction from thinning membranes discussed in this dissertation has been enabled by these synchronous sources.

These analysis tools provide some guidance as to how a QED experiment should be best performed.⁵ Additionally, the crystalline order in most organic monolayers is not extremely long range, ID₂/ID₁ ratios are virtually always present in the beam. The ID values of the ordering also tend to be thermally sensitive. “Bragg rods”²⁸ as opposed to spots are expected. Practically this results in diffraction data of the conventional form (h, k, l) where peaks of order higher than two are rarely observed. As such a typical experiment involves angular ranges of $K_{\text{rod}} \pm 2$ to 2.2 \AA^{-1} and $K_z \pm 0$ to 0.7 \AA^{-1} .

Table 1-1. Some of the synchrotron sources around the world.

Source	City	Energy
APS	Madison, WI	1 GeV
SLAC	Palo Alto, CA	1.3-1.9 GeV
AFS	Chicago, IL	7 GeV
SSRF	Beijing, China	1.8-1.3 GeV
CERN	Geneva, CH	2.5 GeV
ESF	Grenoble, France	1.3 GeV
DESY II	Hamburg, Germany	4.5-1.3 GeV
SOLEIL	Troyes, Italy	1.5-1 GeV
ELIAS	Potsdam, Germany	up to 1.3 GeV
SOLEIL	Grenoble, France	4 GeV
MAX I MAX II	Lund Univ., Sweden	0.05, 1.3 GeV
SLSA	Brookhaven, NY	98 GeV, 1.584 GeV
Proton Factory	Tsukuba, Japan	1.3 GeV, 6.3 GeV
HEPS	Beijing, Korea	5 GeV
SFEL-4	Stanford, CA	2-3.3 GeV
Springs	Japan	8 GeV, under construction
SLSA	Hsinchu, Taiwan	1.3 GeV
SLS	Birmingham, UK	1 GeV
SFEL-3	Novosibirsk, Russia	1.3 GeV

Kjaer *et al.*¹⁰⁰ and Ørskov *et al.*¹⁰¹ were the first to study Langmuir films using a synchrotron source. These experiments observed structure at the intermolecular level and led to the clarification of many misconceptions about Langmuir monolayer phases and phase transitions.¹⁰² Since these initial studies, several experiments have been used at synchrotron facilities. The theory that is related to the grazing incidence X-ray diffraction at the air/water interface is described below.

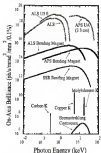


Figure 1.4. Spectral brilliance of some X-ray sources

The critical angle for total external reflection can be calculated using Snell's Law for the geometry shown below:



Snell's Law is

$$n_1 \cos \theta_i = n_2 \cos \theta_t \quad (1-16)$$

where n is the index of refraction, the θ_i is the incident angle, the θ_t refracted angle and $n_1 > n_2$. In this case there will be a critical angle θ_c below which the conditions cannot be satisfied. This is the region of total external reflection. For an air/vacuum interface, n_1 is approximately 1 and equation 1-16 reduces to:

$$\cos \theta_c = n_2 \quad (1-17)$$

The index of refraction, n , can be approximated by,

$$n = 1 + \beta \approx 1 + \frac{4\pi r_e^2 N_A}{\lambda^2} \quad (1-18)$$

where β refers to a small change, r_e is the classical radius of the electron (for water 6.34×10^{-16}), λ is the wavelength of the X-ray beam, and N_A is the classical electron radius (6.02×10^{23}).

As shown in Figure 1-7, X-rays with wave vector k_i are incident on the sample surface at a small angle of incidence θ_i ($\theta_i \approx 0.1^\circ$), where θ_c is the critical angle for

When the incident angle is below the angle of total reflection, the only transmitted wave will be an evanescent wave that decays along the surface. Thus, any diffraction which takes place will be from the surface, and the bulk signal will be negligible. This feature makes grazing incidence geometry very useful for surface studies. In order for the grazing incidence X-ray diffraction technique to work, the beam of X-rays must be highly collimated so that the incident angle is well defined. A dispersed beam would have some fraction of the beam above the critical angle and would contribute a significant background signal. Synchrotron X-rays are both highly intense and highly collimated, which makes them suitable for these types of experiments.

Following is a brief description of the analysis of grazing incidence diffraction, more complete information can be found elsewhere.¹⁰⁻¹² Since the monolayer is monic on the surface, the diffraction pattern is always averaged over all domains translations in the monolayer plane, and any structural information is lost. Out of the three components (k_x , k_y and k_z) of a wave vector \mathbf{k} , only k_z can be directly measured. Even though k_x and k_y cannot be measured separately, the combination $k_{\parallel} = \sqrt{k_x^2 + k_y^2}$ can be measured. If the molecules do not tilt on average, all the peaks lie in the plane of the monolayer. If the two-dimensional crystalline structure possesses six-fold symmetry, all six first-order wave vectors of \mathbf{k} would have equal length and overlap completely in the powder pattern. The single observed peak is highly degenerate. Tilted degeneracy decides when the hexagonal lattice structure is destroyed, which causes distinct peaks at different values of k_{\parallel} . At this point the unit cell is assumed rectangular, where there are two distinct first-order wave vectors. Two pairs with degenerate peaks and one pair with nondegenerate peaks.

The degeneracy may also be affected by the tilt of the molecule, which would result in the movement of the peaks out from the plane of the monolayer by a distance of h_z . This depends on the magnitude and the direction of the tilt. If the tilt of the molecule is towards one of their nearest neighbors (NN)-molecules (Figure 1-B), four peaks move out of the plane of the monolayer, two upward and two downward (downward peaks cannot be observed). The two upward peaks are degenerate in the parallel pattern, that is they have equal k_z values. The tilt angle, α , is given by

$$\sin \alpha = \frac{h_z}{\sqrt{\frac{1}{2}(h_{\text{NN}} + h_{\text{NNN}})^2 + \frac{1}{2}(h_{\text{NN}} - h_{\text{NNN}})^2}} \quad (1-11)$$

When the molecules are tilted towards the next-nearest-neighbor (NNN)-molecule (Figure 1-C), all the wave vectors move out of the plane of the monolayer. There are two distinct values of h_z , where one is twice the magnitude of the other. The tilt angle, α , of the molecules is calculated using the higher h_z value peak, where

$$\sin \alpha = h_z/h_{\text{NN}} \quad (1-12)$$

The work presented in this dissertation tends to investigate much more complex amphiphiles, specifically polymers. X-ray and Neutron scattering experiments of polymers on SiO₂ surfaces have been performed by a number of researchers.¹⁰⁴⁻¹⁰⁷ These experiments have led to important insights on the conformation of polymers at surfaces and how this compares with bulk state. Many other studies have been published regarding CD of polymer monolayers.¹⁰⁸

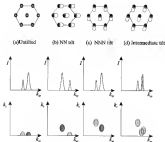


Figure 8: Views of the molecules (first row) and the corresponding intensity distributions (see bottom row) in (a) uniaxial, (b) PM tilt, (c) MPN tilt, and (d) intermolecular tilted phases.²⁷

1.5 Applications of Low-cost and Low-power-Modest Films

Some organic materials have interesting optical, electrical, and biological properties, and methods of modern organic chemistry make it feasible to modify the structure of a given organic material very precisely. By modifying the properties of a compound, one can optimize a particular molecule for a specific application. Although the classical long alkyl chain with a hydrophobic head group has been the major focus of monolayer research, different molecular structures such as porphyrins,¹⁰⁸ phthalocyanines,¹⁰⁹ oligothiophenes,¹¹⁰ and polycyclic aromatic systems¹¹¹ have been reported to form stable monolayers. Much of the recent work done on LB films was focused on photochemical, thermal stability, and "active" physical properties such as electrical conductivity, photoelectric activity, and nonlinear optical properties. The LB films are used in a wide variety of applications, some of which are summarized in Table 1-2.

Gas sensors have been the most studied devices on LB-applications.¹¹²⁻¹¹⁵ When a gas sensor is exposed to the gas of interest, a change in resistance of the semiconducting LB film is measured (link-On reaction).¹¹⁶ Although selectivity is not great, the sensitivities of these devices have been reported to be a few parts per million.¹¹⁷ Semiconducting LB films are used as diodes and LB films have been incorporated into different types of diode structures. Selectivity/barrier conditions can be obtained by using an Ag/AgNO₃ 2-type monolayers of a redox-active compound/Mg junction.¹¹⁸ Another use of LB films is to provide an insulating layer on an opaque semiconducting device.¹¹⁹

Table 1-2: Properties and applications of LB films.^{1,21}

Property	Application
Electrical Conductivity	Chemisorbed Electrochromic display
Insulating properties	Barrier layers in semiconducting devices
Pyrrolic activity	Infrared sensors
Optical anisotropy	Frequency converter and modulator Fast signal processing
Chemical reactivity	Photo- and x-ray resist Information storage

There are many model systems that allowed LB films to research and understand complex systems. Kuhn,²² who pioneered this field, investigated inter-molecular interactions and various photophysical and photochemical properties.²³ Some examples of active research in these model systems are investigations of the energy transfer mechanisms,²⁴ magnetic monolayers,²⁵ biological membranes,²⁶ and permeable²⁷ membranes.

The pyroelectric effect stems as a result of the change in the spontaneous polarization with temperature. The LB multilayers were first used for pyroelectric applications in 1982.²⁸ Initial work was done with X-type LB films, but later Z-type and ohmic layer LB films were used with a wide variety of organic materials.^{29,30}

The field of optoelectronics has been a very exciting research area in the past two decades. The second order nonlinear optical effects (such as second harmonic generation, electro-optic modulation, and frequency up and down) are increasing interest

they can be used as information storage and data signal processing. The general approach in synthesizing nonlinear-optic (NLO) molecules has been to couple a long alkyl chain with an asymmetric dye molecule such as coumarins.¹⁰¹ Although polymeric materials possess excellent nonlinear-optical properties, several investigations were performed on polymerically amphiphiles in order to obtain viable NLO systems.¹⁰²

The field of Langmuir and Langmuir-Blodgett films has been known for 60 years, but during the last two decades, courtesy of a new understanding of the behavior of molecules on a water surface has brought us to the threshold of a new era in molecular science and engineering. The variety of organic molecules, which can be modified in order to obtain desirable properties for use in specific applications, is limitless.

1.6. Conclusions

The first chapter was a brief review of the basic reference and the theoretical concepts that are related to the dissertation. Since the dissertation is based largely on Langmuir and Langmuir-Blodgett techniques, the history and advances of the field was discussed first, and then some general thermodynamic aspects that relate to the field were provided. Much spontaneity was also reviewed so that the reader would gain their idea of the techniques that were used in the dissertation. After the discovery of X-rays in 1895, the field has grown to an extent that it now has third generation synchrotron X-rays, and the use of X-ray has gone through a wide variety of utilizes. Development of the X-ray and the fundamental theory behind the experiments was discussed in this chapter.

The main goal of this chapter was to give the reader a basic understanding of the techniques and the materials used here so that the reader could follow their discussion, regardless of their background. The next chapter explains Langmuir and Langmuir-Blodgett experiments and the results, including some other polymer characterization techniques as well. The Chapter 3 is dedicated to mass spectrometric techniques that were used in the study to obtain information toward the sequence of the copolymers. The fourth chapter discusses structural information, which was obtained employing X-ray diffraction methods. Finally, Chapter 5 concludes the text by describing the grazing incidence X ray diffraction setup which was built at the center of Advanced Photon Source.

CHAPTER 3 CHARACTERIZATION OF THE LANGMUIR FILMS

3.1. Introduction

This chapter reports the general characterization of Langmuir and Langmuir-Blodgett films. The synthesis, polymerization, and thermal properties of 3-benzoyl pyridine (BBDP) and N-methyl-2-pyridyl(NMCP) were investigated. Other analytical techniques such as UV-vis, IR, NMR, and GPC were used to show that polymerization had taken place at the water/air interface.

3.2. Experimental Procedures

3.2.1. Langmuir and Langmuir-Blodgett Films

Langmuir experiments were done in our lab at the University of Florida. Four KSV1000 systems (KSV Instruments, Finland) and one roughness system were used in the records. The KSV1000 rough system can be used with any of the following surface characterization attachments: Wilhelmy or Langmuir surface balance, a dipping unit, a surface potential unit, and a temperature measuring unit. (A standard KSV1000 system is shown in Figure 3-1 with some units attached.) All of the experiments were done with this Sierani with systematic comparisons.



Figure 2-1 KSV-5000 Langmuir trough-system with a dipper and surface balance units attached.

2.1.1.3 Langmuir trough

All of the defined surface characterization units were coupled with the main frame of the KSV-5000, and each device had its own analog-to-digital converter to relay information to the mainframe. The monolayers and the computer were connected via the computer's parallel port. The Langmuir trough was made out of a Teflon piece mounted in a metal base using a special thermally stable glue. The metal base consisted of channels to allow the flow of temperature-controlled fluid through it in order to maintain a specific temperature in the subphase. The bottom of the base consisted of four screws, which could adjust to the level of the trough. The Teflon piece was machined very precisely to have a very smooth surface and a well with a depth about 0.25 mm. A dipping well was in the middle of the trough in order to assist in the dipping.

experiments. The size of the digging well depended on the dimensions of the trough and was typically 3-4 inches deep and about 2 inches wide. One lab owns various troughs with different dimensions, which gave the flexibility of different compensation rates. Each of the troughs was connected to a MelcorTM temperature-controlled recirculating bath, which maintained a constant temperature at the surface. The temperature at the surface was monitored by a Teflon-coated thermometer (±0.1°C) which measured to less than 0.1°C. The trough was placed on a large block of concrete, which was kept on small rollers in order to minimize the vibration transfer from the experimental floor.

Barriers of trough were made out of Teflon (hydrophobic) or Nylon (hydrophilic). The Nylon barriers made an excellent seal at the side of the trough keeping the monolayer in the defined area (see setup). All of the experiments described in this work were done using the Nylon barriers. The barriers were driven by a motor-step motor, which directed its position by an optical encoder within the transducer.

In all the experiments, the surface pressure was measured by the Wilhelmy plate method. The plate was a roughened Platinum (Pt) plate, which was completely wettable when submerged in water. The Pt plate was stored in an absolute ethanol solvent when not in use. Before each use, the plate was heated by the point of being red hot on a Meker burner and being under the balance. The balance contained a photolock, which displayed the movement of the balance arm and returned the height back to the original position. The voltage applied to bring the balance to a reference point was measured, and the data were fed into a 16-bit A/D converter for data processing. The height of the plate, which was submerged in the subphase, was very important since the net force acting on the plate changes with the height.

All the barriers and the troughs were cleaned thoroughly with absolute ethanol and also cleaned several times with pure HEMAfree commercial MilliporeTM water which removes impurities from the subphase contact areas. As a good practice, all troughs were filled with water and kept in a closed environment when they were set in use. First, the barriers were brought to the desired position, and the trough was filled with the subphase. Then, the barrier was hung and secured. Next, the barriers were expanded to the starting position, and the barrier rolling was monitored. If the barrier misaligned the area coating, the surfactant solution could be spread onto the air-water interface. After the experiments were done, all the data were transferred to Adobe format and analysed using OriginTM 4.0 from Microsoft software.

2.1.1.2 Molecular solutions

The KSV program, Isotherm, was used to obtain air solutions of a monolayer film of the KSV programme has a window where you could enter the related experimental parameters such as trough dimensions, the analyte solution concentration and volume, and the molecular weight of the analyte. At the control window of the Isotherm program, the forward barrier speed and target pressure can be configured. All of the solutions, except the polymers, were done in pure HEMAfree commercial MilliporeTM water. According to the solution preparation that is described in section 2.1.4, the surfactant solutions were prepared and were dispensed dropwise using a HamiltonTM syringe over the area of the subphase. The solvent was allowed to evaporate for about 2 min. All of the components ratios were set as approximately

1.1.1.2. *Interfacial tension (γ) experiment with films on steel of polystyrene* When the experiment began, the barriers moved closer at a constant speed, and the confined area decreased, which resulted in an increase of surface pressure that was measured by the surface balance. This same experiment was repeated three times to obtain the associated error and ensure the reproducibility of the system. The error associated with the surface experiment was less than 0.02mN/m for the surface pressure and less than 0.001 $\mu\text{mol}/\text{m}^2$ for the mean molecular area.

1.1.1.3. *Interfacial stability*

Interfacial stability was used to measure the stability of a monolayer at a constant surface pressure with time. First, the analysis solution was spread onto the interface as described in section 1.1.1.1, and the area decreased until a target surface pressure was achieved. Then, the program began to record the value of the mean molecular area (MMR) at a specific time in the initial 10min. Every five seconds the program sampled the rate of mean molecular area that could be used to study the stability of the monolayer.

1.1.1.4. *Hysteresis*

Hysteresis of the monolayer was determined by an automated calculation of the ESR-NMR software. Hysteresis of a monolayer was analyzed to study the thermodynamic reversibility of the monolayer. First, a predetermined surface pressure or

a most molecular area was chosen, and the beam was expanded and contracted at a constant speed (less than $1 \text{ \AA}^2/\text{molecular/area}$) several times in a cycle. At the top and the bottom of the cycle, the monolayer was allowed to relax for two minutes.

2.2.1.3 Langmuir-Blodgett Films

Langmuir-Blodgett (LB) films were made out of the Langmuir monolayers that were described in section 2.2.1.2, and the substrates were prepared as described in section 2.2.1.5. The film studied in this research were T-type, and the substrate was attached to the dipping arm and submerged into the clean water subphase before the monolayer solution was spread. The typical dimensions of the 8x water substrate was 1.8x0.8x0.05 inch. Treated fused monolayers were obtained by an automated combination of the RFX-2000 software called dipping. The dimensions of the substrate and the experimental parameters were entered into the program. When the program was started, the confined area was reduced until a predetermined surface pressure was achieved, and the dipper started the upstroke at an assigned constant speed. The beam continuously moved in order to maintain the surface pressure. At the end of the each stroke (up and down), the substrate was kept on a fixed position. At the end of the upstroke, the substrate was dried for at least 30 minutes. The average transfer ratios (as shown in Equation 1-7) were observed, and only LB films with an average transfer ratio of 0.90 or better were kept for X-ray diffraction experiments. The transferred film was dried in a desiccator for at least 4 hours but for no more than 24 hours.

3.1.1.6 Surface potential

The vibrating plate method was used to measure the surface potential (as described in Section 1.1.2) of the monolayer. The KPF vibrating plate was consisted of a plate that was submerged in the subphase and an audio speaker that stayed above the interface (Figure 3-2). After the water was added to the trough, the speaker was



Figure 3-2. Schematic of the setup for measuring surface potential by vibrating plate method. A, film balance trough; B, platinum electrode; C, potentiometer; D, vibrating plate; E, water proof of the loudspeaker; F, amplifier; G, high resistance ($>10\text{M}\Omega$).

raised or not the surface potential set for values zero. The surfactant solution was spread, and the surface pressure and the surface potential were recorded simultaneously against the monolayer molecular area. After each use, the platinum plate was thoroughly washed with absolute ethanol and pure water.

2.2.1.1 Polymerization at the Interface

Polymerization at the monolayer was observed by an automated calibration of the KSV8000 software called *kinetics*. For polymerization experiments, a different subphase, 0.01% ammonium persulfate, ($\text{NH}_4\text{S}_2\text{O}_8$, reagent) After the subphase solution was spread, the monolayer was compressed immediately at a constant speed of $20\text{Å}/\text{min}$. After the desired surface pressure was achieved, the kinetics program was started and a change of mean molecular area was recorded against the time. After 60 minutes, the program was terminated, the Wilhelmy plate removed, and the barriers were brought very close together, trapping the collapsed monolayer between them. The sample was scraped out using a metal spatula and dissolved in 10 mL of chloroform. After collecting multiple steps of the same sample, the chloroform solution was thoroughly washed with pure water (the solvent evaporated), and the final product was dried in a desiccator for 24 hours before further characterization of the polymer (as explained in sections 2.2.2 through 2.2.4)

2.2.1.2 Brewster Angle Microscopy

The Brewster Angle Microscope (BAM) (Figure 3-19) was a separate unit from the KSV instruments, and each was operated independently. The BAM was purchased from Molecular Imaging™, Germany, and it was not of the first generation. The BAM was arranged to fit above the Langmuir trough, as seen in Figure 3-1. The laser beam was set to the p-polarization, and the angle of the incoming beam was set to the Brewster angle with respect to the air/water interface. The objective of the microscope

was adjusted to view the image through the highly sensitive Sony CCD camera. All of the lenses consisted of smoothly polished glass cylinders with a thin layer of gold on them. The analyzer unit consisted of a polarizing filter, which could be adjusted to a desired polarization direction and was able to pull in or out of the optical path to investigate the anisotropy of the interface, especially with polarizable monolayers. The microscope unit could be moved in all three x - y - z axes, which was useful to reach most parts of the monolayer to observe the difference. The signal from the CCD camera was sent to a video integration unit and then to a VTR to record the image and to a monitor to view the real time images. The microscope was operated as described in section 2.2.1.3 and the software routines was run in the RRT program with additional parameter, *time*. By having the time and the surface pressure against MMA, and by beginning the isotherm process and the recording of the video simultaneously, one could know the surface pressure of the corresponding image.

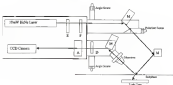


Figure 2-3 Schematic of Brewster Angle Microscope.

1.1.1 UV-Vis Spectroscopy

The UV spectra of monomers and copolymers were obtained from chloroform solutions on a Varian-Cary 50 UV-Vis-NIR spectrometer.

1.1.2 IR Spectroscopy

IR spectra were recorded using an FTIR-40A FTIR spectrometer (Jin-Rui Lab MA). The Fourier transform infrared spectra were obtained using a Biotek FTIR dual with the diffuse reflectance attachment. The samples were mixed with dry KBr and loosely packed into the sample holder.

1.1.4 NMR Spectroscopy

All NMR spectra were performed using a Varian VXR 300 spectrometer in deuteriochloroform as solvent. Tetramethylsilane (TMS) was used as the internal reference. ^1H NMR experiments were done for 64 repetitions at 300KHz, and ^{13}C experiments were done for 4096 repetitions at 75MHz.

1.1.5 Gel Permeation Chromatography

Gel permeation chromatography (GPC) data were collected using a Waters Associates liquid chromatograph apparatus equipped with a LHR injector and UV spectrophotometer detector from Poltek Chem. The sample studied was obtained by

confirming the results of two monolayers polymerized under the same conditions. Two photoreactors T-4 and a 300 nm Photocell 5 commercial fluorescent tubes were used, a 300 Å, followed by a 1800 Å type. The eluting solvent was HPLC grade THF at a flow rate of 1.0 mL/min. Retention times were calibrated using polystyrene standards. It should be noted that since the sample consisted of a mixture of several runs and no calibrations using better standards were possible, the absolute values of the molecular weights are likely to be indicative.

2.2. Monomers

2.2.1. *N*-acetylsulfolene

N-acetylsulfolene (NACS) was purchased from TCI America, Inc., and the purity of the compound was only 98.9% (by GC). After a flash chromatography (with stationary phase, silica gel, mobile phase, 10 : 1 petroleum ether : ethyl acetate), 99.9% purity was obtained.

2.2.2. 3-(*N*-acetylsulfolene)pyrrole

Synthesis of 3-(*N*-acetylsulfolene)pyrrole (NACP) was based on a four-step reaction, which had been previously published.¹⁶ Step 1 of the reaction was to add a protecting group to the nitrogen position (Figure 2-6). First, pyrrole (bp = 33.1 °C) was distilled (colorless liquid). Potassium was washed with petroleum and weighed 3.05 g in a petroleum solution. The potassium was added to the reaction flask, which had an Argon purge, and

distilled tetrahydrofuran (THF) was added. Using a disposable syringe, 10 mL of distilled pyridine was added through a rubber septum. The mixture was refluxed gently until all the potassium had reacted. As the magnet stirring was discontinued, and the reaction stopped bubbling and was a pale pink slurry. The mixture was diluted with 100 mL of tetrahydrofuran and, using an addition funnel, 100 mL of TM acetyl chloride in tetrahydrofuran was added dropwise for about 30 minutes. After the reacting mixture had been stirred at room temperature for about 18 hours, it was filtered to yield a solution, which was evaporated at 35°C in a rotary pump. The solid was dissolved with 40 mL of methanol and heated to 35°C using a water bath. The flask of the solution was submerged in an ice water bath to obtain crystals, which were dried at a vacuum oven at room temperature. The product was kept out of light until the next step. The 3-isopropenyl crystals were white in color, were needles, and had a melting point of 50.5-100.2 °C. The yield of the product was 89%. Both TLC and GC showed only one product. The ¹H-NMR (CDCl₃) δ: 4.5 (s, 1H, CH₂), 4.34 (dd, 2H, H-C-CH₂), 7.28 (dd, 2H, H-C-CH₂), 7.34 (dd, 1H, CH₂-C-CH₂), 7.77 (dd, 2H, H-C-CH₂) and ¹³C-NMR (CDCl₃) δ: 21.0 (CH₃), 115.46 (CH-CH-CH₂), 128.51 (H-C-CH₂), 128.40 (H-C-CH₂), 129.88 (H-C-CH-CH₂), 134.81 (H-C), 146.84 (CH₂-C) spectra were obtained with a Varian VXR 300. Elemental analysis of 3-isopropenyl was as follows: Calculated: C, 79.51; H, 5.61; N, 4.70; S, 14.48. Found: C, 78.81; H, 5.15; N, 4.52; S, 14.18.

Step 3 of the reaction was Friedel-Crafts acylation of 3-isopropenyl. Distilled methylene chloride (100 mL) added to 7.5 g (34.94 mmol) of aluminum methoxide which was suspended under argon. A solution of 15.4 mL (34.94 mmol) of acyl chloride in 25 mL of distilled methylene chloride was slowly added at 0°C, and the mixture was stirred

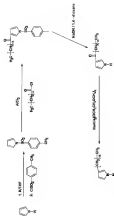


Figure 2.4 Synthesis route to 3-benzimidazolyl pyridine

for 18 more minutes. The mixture was kept at 3°C when adding 15.67g (49.87 mmol) of 1-terephthale dissolved in 250ml, distilled methylene chloride. After an additional 2 hours of stirring at ambient temperature, the reaction mixture was treated with ice water. Caution was exercised to add ice-water slowly, otherwise vigorous bubbling would have caused product to be lost. The product was extracted with methylene chloride and dried with sodium sulfate. The filtered solution was evaporated, and the product was recrystallized twice using 100ml, of methanol each time. The product was dried in the vacuum at 40°C for 4 hours. The 1-terp 3-benzotriazene pyridine crystals were white in color, were granular and had a melting point of 99.2/100.2 °C. The yield of the product was 47%. Both TLC and GC showed only two substances, and the other was the unreacted 1-terephthale. The ¹H-NMR (CDCl₃) δ 8.03-8.10, 1H, CH₂-CH₂, 1.20 (m, 24H, internal alkyl-CH₂), 1.73 (m, 1H, CO-CH₂-CH₂), 2.40 (s, 3H, C-CH₃), 3.70 (t, 2H, CO-CH₂), 4.70 (d, 1H, H-CH-CH₂), 7.28 (m, 2H, CH₂-C-CH₂), 7.35 (s, 1H, N-CH-CH₂), 7.61 (d, 2H, S-C-CH₂), 7.66 (s, 1H, H-CH-CH₂) and ¹³C-NMR (CDCl₃) δ 14.04 (CH₃-CH₂), 21.38 (C-CH₂), 23.41 (CH₂-CH₂), 24.28 (CO-CH₂-CH₂), 26.37 (internal alkyl-CH₂), 31.34 (CH₂-CH₂-CH₂), 36.70 (CO-CH₂), 111.31 (H-CH-CH₂), 121.37 (H-CH-CH₂), 122.65 (H-CH-CH₂), 127.12 (S-C-CH₂), 128.21 (S-CH₂), 130.23 (CH-C-CH₂), 135.51 (H-CH-CH₂), 141.32 (C-CH₂), (51-61) (CDCl₃) spectra were obtained with a Varian VXR 300. Elemental analysis of 1-terp 3-benzotriazene pyridine was as follows: Calculated C, 76.15; H, 5.08; N, 3.48; S, 4.37. Found: C, 76.11; H, 5.03; N, 3.43; S, 4.37.

The next step was to remove the protecting group. Add 15.13g (44.87 mmol) of 1-terp 3-benzotriazene pyridine to 250ml, of 1,4-dioxane and stir in 250ml, of 30% sodium hydroxide. The mixture was refluxed for 24 hours. The phases were separated,

and the aqueous layer extracted with diethyl ether. The combined organic layers were washed with a saturated sodium chloride solution and dried over anhydrous sodium sulfate. The solution was evaporated, and the product was recrystallized with diethyl ether. The 3-benzodioxane pyridole was white in color, was waxy, and had a melting point of 76.1–76.4°C. The yield of the product was 83%. Both TLC and GC showed only one substance. The $^1\text{H-NMR}$ (Figure 2-6) (CDCl_3) δ 1.56 (s, 3H, CH_3), 1.24 (m, 24H, internal alkyl- CH_2 's), 1.40 (s, 3H, $\text{CO-CH}_2\text{-CH}_3$), 2.44 (t, 3H, CO-CH_2), 5.74 (s, 1H, H- CH-CH_2), 6.87 (s, 1H, H- CH-CH_2), 7.34 (s, 1H, H- CH-CH_2), 9.42 (s, 1H, H- N) and $^{13}\text{C-NMR}$ (Figure 2-6) (CDCl_3) δ 14.67 (CH_3), 22.64 ($\text{CH}_2\text{-CH}_3$), 25.23 ($\text{CO-CH}_2\text{-CH}_3$), 29.64 (internal alkyl- CH_2 's), 31.47 ($\text{CH}_2\text{-CH}_2\text{-CH}_3$), 39.74 (CO-CH_2), 100.80 (H- CH-CH_2), 113.64 (H- CH-CH_2), 125.81 (H- CH-CH_2), 129.47 (H- CH-CH_2), 158.6 (CO) species were observed with a Varian VXR-500. Elemental analysis of 3-benzodioxane pyridole was as follows: Calculated, C, 78.63, H, 11.55, N, 4.58. Found, C, 78.43, H, 11.36, N, 4.58.

The fourth step was to reduce 3-benzodioxane pyridole to obtain 3-benzodioxol pyridole. In distilled tetrahydrofuran, 10 g (28 mmol) of red aluminum (Al) ($\text{AlH}_3(\text{OCH}_2\text{CH}_2\text{OCH}_2)_3$) were suspended under nitrogen. While cooling with ice water, 4 g of 3-benzodioxane pyridole were added in small portions. The resulting mixture was stirred for 3 hours at room temperature and then heated for an additional hour at 30°C . After cooling to ambient temperature, water was added cautiously and extracted with diethyl ether. The extracts were dried over anhydrous sodium sulfate, and the solvent was distilled off. From a single fractioned distillation was suggested, 95.26% purity (by GC) was obtained after a flash chromatography and a thin layer chromatography (preparative plate), and the compound was used as it was given. The 3-benzodioxol pyridole was waxy

white solid and had a sharp melting point at 45–46 °C. The yield of the product was 80%. Also $^1\text{H-NMR}$ (Figure 3-5) (CDCl_3) δ 1.10 (s, 3H, CH_3), 1.88 (m, 2H, internal alkyl- CH_2), 1.41 (m, 2H, $\text{py-CH}_2\text{-CH}_2$), 2.71 (s, 2H, py-CH_2), 4.31 (s, 1H, N-CH- CH_3), 4.76 (s, 1H, N-CH- CH_3), 4.88 (s, 1H, N-CH- CH_3), 4.90 (s, 1H, N- CH_3) and $^{13}\text{C-NMR}$ (Figure 3-6) (CDCl_3) δ 15.09 (CH_3), 22.66 ($\text{CH}_2\text{-CH}_2$), 26.75 ($\text{py-CH}_2\text{-CH}_2$), 31.06 (py-CH_2), 31.74 ($\text{CH}_2\text{-CH}_2\text{-CH}_2$), 106.31 (py-CH), 104.59 (py-CH), 117.33 (py-CH), 104.43 (py-CH) peaks were obtained with a Varian VXR 300, and they agreed with the literature values. Elemental analysis of **3HDP** was as follows: Calculated: C, 62.40; H, 12.76; N, 4.84. Found: C, 62.36; H, 12.73; N, 4.82.

3.3.3. Cleaning Procedures

Before preparing Langmuir-Blodgett, the trough was cleaned thoroughly as follows: First, the trough was filled with Millipore water and cleaned several times. Then, all the Teflon parts were cleaned with Kimwipes, which were wetted with absolute ethanol and then with chloroform. The trough was then filled with Millipore water and checked for impurities by measuring the surface pressure with changing area. Between runs the trough and the barriers were cleaned twice with Millipore water and wiped with Kimwipes soaked in chloroform.

Impurities are very much a concern when the Langmuir technique is used since any surface-active impurities will end up at the interface and interfere with the monolayer characterisation. All of the water used in the cleaning was taken from the Millipore Pure Ultrapure water system, which offers water with 18 M Ω cm resistivity, with low organic ($<10\text{ppb}$), free of macroorganisms ($<1\text{ bacteria/L}$), and free of particles ($<0.2\text{ bacteria/L}$). All

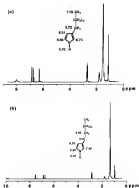


Figure S-8. ^1H NMR spectra of monomers: (a) 3-benzoyl glycidol and (b) 3-iodobenzoyl glycidol in CD_2Cl_2 .

of the glassware was cleaned as follows: The glassware was submerged in a fresh *Sulfosoma*TM and 6N H_2SO_4 solution for 3 hours. The glassware was then washed with Millipore water five times, filled with pure water and sonicated for 30 minutes. The glassware was again rinsed five more times with Millipore water.

Gas-tight microsyringes were purchased from Hamilton and cleaned with chloroform in a sonicator for one hour. Before syringes were used, they were again rinsed with Chloroform five times and twice with the analyte solution. In between uses, they were filled with chloroform. A Teflon tube, which lightly fits the syringe needle, was attached to help spread the solution at the interface and also to achieve reproducibility.

2.1.4. Solution Preparation

All the glassware was cleaned (as described in Section 2.1.3) and stored before making any solutions. Sulfaphase solutions were made using Millipore water and ammonium persulfate, $(NH_4)_2S_2O_8$, which was bought from Aldrich, and used without any further purification. All the sulfaphase solutions were freshly made to ensure purity of the sulfaphase and for reproducibility.

The surfactant analysis and stock solutions were made in Hexil and Dodec, respectively, using 100 μ l syringes. Both stock and analyte solution concentrations were approximately 6.4 mg/ml, and prepared by dissolving the pre-weighed solid with chloroform (approx. 400 μ l, 400 μ l). The analyte solutions were made using the stock solutions and microsyringes (100 μ l to 100 μ l). Using a speedometer and

the formulas below, the concentrations and the molecular weights of the mixed solutions were calculated

$$C = \frac{\sum C_i F_i}{\sum F_i} \quad (3-10)$$

$$MW_{\text{mixture}} = \frac{\sum C_i F_i}{\sum C_i F_i} \quad (3-11)$$

$$MW = \sum MW_{\text{mixture}} \times MW_i \quad (3-12)$$

where C_i , F_i , and MW are concentrations, volume, and molecular weight. All the solutions were stored at the refrigerator and kept away from light by wrapping them with aluminum foil.

3.1.5. Solid Substrate Preparation

All of the solid substrates were made out of silicon (111) wafers, which were purchased from Semiconductor Processing Company. They were cut into desired sizes and immersed in a "piranha" solution (pure H_2SO_4 , 50% H_2O_2 , 70:30 v/v) at 80°C for 1 hour. After cooling to room temperature, they were rinsed repeatedly with Millipore water. They were soaked in another solution, H_2O , 50% H_2O_2 , NH_4F , 5:1:1 v/v/v, at room temperature for 40 minutes. The substrates were then washed with copious amounts of Millipore water and dried by flowing nitrogen gas. They were submerged in a solution of hexane (Mathco, ultrapure) and octadecyltrichlorosilane (OTS) (Chemical Technologies, Inc., 99%) in the ratio of 1:50 v/v for 30 minutes. After washing them with hexane, water drops were added to the substrate surface and the contact angle,

which was not used to measure the surface modification. All substrates with a contact angle of 90° or above were stored under heptane until they were used.

2.4. Langmuir Monolayer Characterization

2.4.1. Isotherms

Isotherms of Langmuir monolayers were obtained according to the procedure described in Section 2.2.1.3.

Pure MDDP is insufficiently amphiphilic to form stable monolayers at all but very low ($< 5 \text{ mN/m}$) pressures. The stability of a monolayer is very important in order to transfer them to a solid substrate for various applications. MDDP mixes well with JEOP to form well behaved, stable monolayers with reduced collapse pressure as shown in Figure 2-7, below. In fact, from the pressure vs. area isotherms of the mixtures, it can be seen that the MDDP actually reduces the surface area occupied by the mixed molecules, thus improving packing compared with the JEOP alone. Langmuir films of JEOP were very stable (by isotherm and loop test measurements) with an onset around 25 mN/m and a collapse pressure of 40 mN/m . This value is comparable to that obtained for the 3-oxadecylpyrene¹²⁸ and a previous investigation of the 3-iodadecylpyrene at different conditions. However, MDDP is not amphiphilic enough to make a stable monolayer above 4 mN/m , and it has a higher onset of 41 mN/m . The higher onset value and the low collapse pressure suggest that pure MDDP forms a monolayer with very poor properties. First, we were not sure whether MDDP was forming monolayers on the interface at zero pressure or not. (If this is true, monolayers

(polymer cannot be obtained). Thus, by using the Brewster angle microscope (Section 2.4.3) and lyotropic (below Au/NaCl), we confirmed that there were no domains before the surface pressure was applied and also confirmed the homogeneity of the monolayer before collapse. Isotherm data are summarized in Table 2-1.

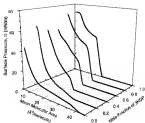


Figure 2-1. Monolayer isotherm-collapse of HSDP/HODP mixtures at 23°C.

Table 3-1 Important values extracted from Figure 3-7.

Mole fraction of HEDP	Onset Value ($\text{\AA}^2/\text{molecule}$)	Collapse Pressure (mN/m)	Area at Collapse ($\text{\AA}^2/\text{molecule}$)
0.0	23.6	45.7	28.5
0.2	24.6	39.3	28.3
0.4	24.4	34.1	28.3
0.6	24.3	32.9	28.3
0.8	23.3	2.6	29.8
1.0	43.6	6.3	37.4

The two monomers (HEDP and NOEDP) mixed with each other very well, and the monolayers of the mixtures were stable, but collapse pressure decreased with increasing mole fraction of NOEDP. At 80%, 90%, and 95% HEDP mixtures had lower on-set values than 100% HEDP, suggesting better lateral order when NOEDP was incorporated with HEDP. We have investigated pure HEDP and the 50% mixture by synchrotron X-ray diffraction, which indicated reduction of the tilt angle of the long alkyl chain with increasing NOEDP mole fraction (Section 4.1.5).

Just as with HEDP, nitrogen on NOEDP had a slightly negatively polar charge, but it could not interact with water freely because of the long alkyl chain attached to the nitrogen position. The pyridine ring seemed to have very little interactions with the water. This can be seen from the low collapse pressures of the pure NOEDP monolayers. The larger onset value of $41 \text{ \AA}^2/\text{molecule}$ could be attributed to the pyridine ring orientation at the water/air interface. As the mole fraction of HEDP increased, the NOEDP molecules were incorporated in the mixed monolayers under the dispersion forces between long alkyl chains dominated in this situation. Since the interactions between water and NOEDP was low, NOEDP did not contribute to the strength of the mixed monolayers. This was evident

from the results—as the HODP mole fraction increased, the collapse pressure of the mixed monolayers decreased.

Table 2-2 Important values extracted from Figures 2-4.

Mole fraction of HODP	Temperature (°C)	Desert Value ($\text{\AA}^2/\text{molecule}$)	Collapse Pressure (mN/m)	Area of Collapse ($\text{\AA}^2/\text{molecule}$)
1.0	20	25.4	41.3	21.2
1.0	21	25.1	44.7	21.8
1.0	25	25.2	43.4	21.1
1.0	27	25.8	43.7	20.2
1.0	30	26.1	44.4	20.5
0.9	15	26.4	43.8	20.6
0.9	22	26.9	42.0	21.2
0.9	26	26.1	39.9	21.0
0.9	27	26.0	38.3	21.2
0.9	28	25.2	33.0	20.7
0.9	30	26.1	31.3	20.6
0.9	34	26.4	34.2	21.2
0.9	36	26.1	29.8	21.2
0.9	38	26.4	28.1	21.2
0.9	40	26.2	28.0	21.4
0.9	43	25.8	25.0	20.9
0.9	44	26.1	20.1	21.2
0.9	50	26.0	22.3	21.2
0.9	52	26.8	32.0	21.8
0.9	56	26.0	8.5	21.8
0.7	18	26.2	34.8	21.2
0.7	19	26.0	30.9	20.2
0.7	26	25.6	3.7	22.8
0.7	28	25.2	3.8	24.9
0.7	38	26.4	3.0	22.4
0.5	19	22.1	3.0	19.8
0.3	12	26.2	25.4	20.6
0.3	25	26.2	3.2	18.9
0.3	28	45.8	4.3	10.4
0.0	28	48.2	1.7	21.9

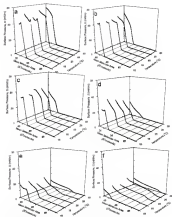


Figure 2.8 Isotherms of mixtures of 3BDP and NBDP at different temperatures. (a) Pure 3BDP, (b) 40% 3BDP and 60% NBDP, (c) 60% 3BDP and 40% NBDP, (d) 80% 3BDP and 20% NBDP, (e) 20% 3BDP and 80% NBDP, and (f) pure NBDP

The temperature of the subphase affects the area occupied by these molecules (Figure 2-8). All of the valuable parameters that were obtained from these Figures are summarized in Table 2-2. The temperature variation from 18-28°C had very little effect on pure TEGP. The “snap-collapse” of SEDP at lower temperatures forms an elongated with higher temperature indicating that the fluidity of SEDP had increased. But with the higher mole fraction of HQGP, there was a clear phase transition with change of temperature. This could be related to aggregation of vesicular molecules together. In the next section we discuss the stability of the monolayer.

2.4.3. Isobaric Stability

The isobaric stability of each pure component was determined using the procedure described in Section 2.2.1.3. The measurements were done at 28°C. The pure TEGP was very stable at pressures of 5, 10, 15, and 20mN/m and lost less than 2% of the initial area in a time period of 120 minutes. These results suggested that pure TEGP forms a very stable monolayer at the water/air interface.

Since pure HQGP has a very low collapse pressure, isobaric stability of HQGP was done at 2 and 5mN/m. At 5mN/m, monolayer loss was close to 2% of the initial area, but at 2mN/m, it lost 20% of its initial area during 120 minutes, indicating instability of the monolayer.

2.4.3. Expansion

The hysteresis of the pure HEDP and MOEP was determined employing the method described in Section 2.2.1.4. The measurements were done at 15°C. Since pure MOEP collapsed at -4.7mPa, it had little or no hysteresis under 1mPa. When the upper surface pressure limit was set to 1mPa, there was a very large hysteresis (about $10 \text{ Å}^2/\text{molecule}$). The large value can be attributed to collapse of the monolayer. The pure HEDP had very little hysteresis ($\sim 0.5 \text{ Å}^2/\text{molecule}$) when performed under the collapse pressure (upper limit was 41mPa).

After polymerization, the monolayer can be characterized by hysteresis expansion, that is, the monolayer is repeatedly expanded and compressed. The homopolymer of 3-hydroxypropylate had a large hysteresis on a subphase containing 0.001 M of ammonium persulfate, as shown in Figure 2-9.

When the monolayer was expanded, an increase in surface area of about $1 \text{ Å}^2/\text{repeat}$ unit was observed for the polymerization product on the ammonium persulfate subphase. The same was true for the co-set point of the first compression of the polymerized monolayer. This result is contradictory since during polymerization the area of the monolayer decreased. The apparent contradiction may be explained if the polymer is assumed to be in a ordered monolayer form after polymerization but rearranged to form lobes of rigid molecule sections during on the water surface. This type of ordering has been seen for other substituted rigid polymers such as C_{60} and is consistent with both the reported tendency of the pyridine backbone to form a helix and the reported helix rearrangement seen as the expansion/contraction

cycles. The conformation adopted by the polymer after the compression cycles may not be the same as that of a monolayer of conventional low molar mass surfactants.

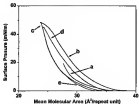


Figure 1-4. Hysteresis of the polymerized monolayer produced of 3-bromododecane. Substrate was 0.01% M sodiumhexafluoroborate. Surface pressure of polymerization was constant at 20 mN/m. a) expansion of the monolayer directly after polymerization, b) first compression, c) re-expansion, d) compression, e) re-expansion.

In a binary mixture, the two components sometimes phase separate and alter the desired physical and electronic properties of the monolayer. In this study, we investigated how the temperature affects the physical properties of the monolayer such as compressibility and excess area of mixing.

3.4.4 Compressibility and Interfacial Area of Mixing

The compressibility and interfacial area of mixing were calculated as shown in Section 1.2. These two properties of the film were calculated only when the film was in a thermodynamically equilibrium state. Since HCOF had very low collapse pressures at all temperatures except 10°C, interfacial area of mixing was calculated (Equations 1-19) at 10°C and only at surface pressures of 1, 3, and 7 mN/m. The positive deviation of this property suggests that tendency of phase separation of the two components. According to the data (Figure 3-10), with an increase in HEDF mole fraction, the tendency was close to ideal.

The compressibility gave a notion about the rigidity of the film. The higher the compressibility of the film, the lower the rigidity of the film. This property of the film is very important since rigid films are very difficult to transfer to a solid substrate. Since these calculations (Equations 1-12) were done at $\Pi = 10$ mN/m, the films with a lower collapse pressure were selected. Two major trends were observed (Figure 3-11). With an increase in temperature, the film was softer. This could be attributed to an increase in kinetic energy of the molecules, which is analogous to melt in the 3-dimensional world. Also, with increase in HEDF, the film became more rigid. Since HEDF was a good amphiphile and HCOF was a weak amphiphile, the rigidity of the film was dominated by HEDF. In a mixed film, HCOF stayed delipidized but still was incorporated in the film via van der Waals-polar interaction of the long alkyl chains. The lack of interaction between HCOF and the water surface caused the compressibility of the film to increase with an increase in HCOF mole fraction.

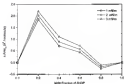


Figure 3-10 Excess area of mixing at 0°C

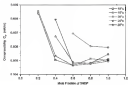


Figure 3-11 Dependence of temperature and mole fraction on compressibility at $T = 100/\text{MPa}$

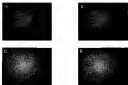


Figure 2-12 BSM images of MOEP: A, $JD = 2 \text{ mN/m}$, B, $JD = 4 \text{ mN/m}$, C, $JD = 20 \text{ mN/m}$, D, $JD = 100 \text{ mN/m}$.

2.4.5. Forward Angle Microscopy

Forward angle microscopy (FAM) pictures were obtained as described in Section 2.2.1.2. The main reason for observing the FAM picture was to investigate the homogeneity of the pure MOEP film before its collapse. Pure MOEP forward angle microscopy images (Figure 2-12) showed homogeneous film lacking any features, which is indicative of a one-phase fluid monolayer.

2.4.6. Surface Potential

Surface potential was measured as described in Section 2.2.3.4, and the dipole moment was calculated as described in Section 1.1.2. The results of the dipole moment are shown in Figure 2-13, and the pressure dependence of dipole moment is shown in

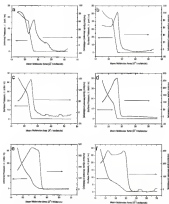


Figure S-13 Surface potential of monolayers at 23°C: (a) Pure THCP, (b) 10% THCP and 90% HODCP, (c) 10% THCP and 90% HODCP, (d) 50% THCP and 50% HODCP, (e) 20% THCP and 80% HODCP, and (f) pure HODCP.

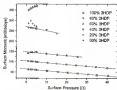


Figure 3-14 Surface dipole moment, μ , vs. surface pressure, Π for monolayer monolayers at 23°C.

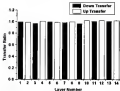


Figure 3-15 Longitudinal/diagonal transfer of pure 2-hexadecylthiol paraffin onto hydrophobized silica wafers. Transfer ratios for the dipping of first 14 layers are shown here.

Figure 2-14. The slopes of Figure 2-13 plots are as follows (units are mDynes/cm²): 100% HEDP = -0.83, 80% HEDP = -0.83, 60% HEDP = -0.89, 40% HEDP = -0.93, and 20% HEDP = -1.48. The small increase in dipole moment from pure HEDP to 80% mixture could be due to a larger change of the molecular orientation of HEDP. This trend was followed until a 40% HEDP mixture, but the positive deviation of the dipole moment of 20% suggested that the orientation of the molecules in a totally different arrangement than in previous cases. The lower collapse pressure of 20% of the HEDP mixture would not allow us to investigate the behavior further.

2.6.2. Langmuir/Blodgett Films

The transfer of monolayers onto solid substrates gave the following results. Different substrates (glass, silica-water, hydrophobic and hydrophilic), dipping speeds (0.5-70 cm/min), applied surface pressures (3-40 mDynes/cm²), time of drying (5-3000 seconds) were examined. Most of the compounds or their polymers could be transferred successfully onto hydrophobic substrates. The monolayers could not be transferred because, on subsequent dipping, the layer was transferred back to the water surface. This behavior was independent of the surface pressure and dipping speed. Therefore, the substrates were made hydrophobic, and the monomer monolayers could be transferred from water successfully.

For the polymers the transfer was done directly from the subphase that was used for the polymerization. If another subphase were used, only a monolayer could be transferred onto hydrophobized substrates. The same was observed when the subphase

pH was increased with ammonia. Therefore, polymerization was done with acetate solutions containing only ammonium persulfate. The rigidity of the polymer monolayer could have hindered the polymerizing transfer to the substrate. Also it is known that rigidity of a film increases when small amount of electrolyte is present (as has been 0.01M ammonium persulfate).

Transfer of monomer monolayers was possible. The transfer ratio (T_r)-depended on the applied surface pressure, surface of the substrate, drying time at an end of a stroke, and dipping speed. The conditions for transfer at 25°C were dipping speed of 4mm/min with a surface pressure of 15mN/m, transfer speed of 2.4×10^{-2} molecule²/minute⁻¹, and the drying time of 1 minute. Only pure HEDP (Figure 2-15), 40%, and 60% of HEDP were successfully transferred. The monolayers of 40%, 20% and pure HODP were too mobile enough to reach the surface pressure needed for the transfer.

Under these conditions subsequent dipping apparently resulted in T-type multilayers as shown in Figure 1-3. STM investigations on transferred polymer monolayers of these compounds have shown no evidence of polymer chain overlap, which is an additional indication of the 2-D nature of the polymer chains formed.¹²

2.3. Langmuir Monolayer Polymerization

The pure HEDP monolayers can be polymerized to a low molecular weight (MW) (Figure 2-16 Below). Because of instability to applied surface pressure, HODP is not effectively polymerized by these methods. Surprisingly, mixtures of these two monomers are polymerizable, yielding well-ordered monolayer products. Both cases of

The polymers in Figure 3-14 show that they result in more stable films, with different surface areas, than the corresponding monomers.

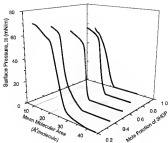


Figure 3-14 Isotherms of polymer after racing at $T=250\text{K/min}$ and 1PC

Previous studies, except recent publications,¹⁷⁻¹⁹ have shown that MDP at surfaces can be polymerized to thin films (though not monolayers) by initiating large amounts of unanchored pyridyl monomer in the substrate¹⁷ or through initiation with a self-assembling monolayer,¹⁸ however, no sequence control was studied. Both monomers are polymerizable in solution by conventional methods.¹⁷⁻¹⁹ We suppose that surface orientation imposed in the monolayer should significantly affect how the monomers in a mixture react and incorporate in monolayer-thick copolymers compared with bulk solution polymerized material. By polymerizing monolayers, we hope to demonstrate control of copolymer sequence distributions not obtainable by conventional reactions.

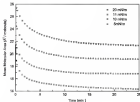


Figure 3-17 Polymerization of pure MDP at 25°C

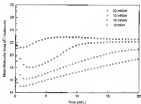


Figure 3-11. Polymerization of 50% mixture of HEDP and HODP at 15°C.

The copolymer monolayers were prepared by spreading the monomer solutions on a 0.01 M ammonium persulfate subphase. The polymerization was performed at a constant surface pressure of 20 mN/m for 15 min. After the polymerization was complete, the currents were turned off, and the surface pressure was allowed to equilibrate before the isotherms were recorded. When a monomer monolayer is under pressure, the molecules are within their van der Waals distance. When polymerizing, that van der Waals distance is replaced by a covalent bond which we can observe by monitoring the change in area with applied constant surface pressure (Figure 3-17,18). The greatest amount of area change is in pure HEDP. In fact, when the surface pressure is 20 mN/m,

the mean molecular area reduces to ~ 64.5 Å²/molecule and when a neat monolayer cannot exist (Figure 3-17). This suggests that the backbone of the polymer might be coming off the substrate interface. Hopefully, this change could be verified by synchrotron X-ray diffraction. Also, less understood is the dp (Figure 3-18) at 60% and 90% HEDP. It is certain that HEDP influences this area change, but we are very interested in knowing what kinds of changes (in terms of the molecular packing) are occurring on the first two monomers of the polymerization.

The polymers all show increased and similar collapse pressures of 30-40 mN/m (0.01-0.04 mN/cm²) parallel to the surface compared to the collapse pressures of the monomer monolayers.

3.4 Characterization by Standard Polymer Techniques

3.4.1 UV-Vis Spectroscopy

Figure 3-19 shows the UV-vis spectra of 3-benzoylpyridine (curve a) and its product after the polymerization on the LB-surface (curve b). The HEDP monomer had UV-Vis spectra with one absorption band at 230nm. However, in other regions the UV-Vis spectra of the homopolymers of HEDP was completely different from the monomer and showed a broad absorbance in the range of 200nm to 600nm with a peak at 400nm and a plateau at and beyond 400nm. An additional peak at 230nm might be attributed to unreacted monomer that is left in the product. The optical spectra of the obtained material clearly indicate that polymer is formed. The spectra are in good agreement with those of poly(3-alkyl pyridine)s at intermediate degrees of oxidation.¹²⁸ Indeed, the color

of the polymer in chloroform was dark greenish, unlike the dark black color of initial polypyrrole.¹²⁸ If the polymer formed was left on the trough under air for several hours, further oxidative degradation of the poly(3-allyl pyridine) occurred which decreased the polymer yield and caused the color of the products to turn brown, and smaller molecular weights were measured. This also agrees with the behavior of polypyrroles synthesized by conventional means, where only highly reduced material is stable under ambient conditions. With a decreasing degree of oxidation, the stability strongly decreases, and neutral polypyrrole derivatives degrade in air almost instantaneously.

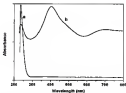


Figure 3-15 UV-vis spectra of (a) 3-allylpyridine and (b) its polymerization product from the C3b trough in chloroform solution.

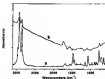


Figure 3-10 IR spectrum of (a) 3-benzothioyl pyridine and (b) its monolayer polymerization product in KBr

3.6.3 IR Spectroscopy

The IR spectrum (Figure 3-10) is in good agreement with that of poly(3-allyl pyridine) synthesized by electrochemical or conventional systems with thiolate chloride as initiator.¹⁰⁰ However, it should be noted that highly oxidized material, such as polymer obtained by electrochemical means, shows a strong IR absorption at 4000 to 1800 cm^{-1} . The broad ferrocene band has been attributed to a free charge carrier absorption. In highly-oxidized material, in fact, the intensity of that band is so strong that it completely covers the bands due to the C-H vibrations of the allyl side chain. In the material synthesized as described here, the bands due to vibrations in the side chains are still visible. A band at 1730 cm^{-1} wavenumber indicates that some of the pyridine moieties were

also oxidized (C=O stretch). We expect this to be only a minor amount since the NMR does not indicate any additional compounds other than the regular structure, and the oxidized moiety is known to have a very high extinction coefficient. These results are in agreement with corresponding studies of oxidized material in the bulk.¹²⁰

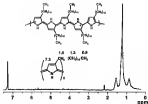


Figure 2-11. ^1H -NMR spectrum of L-aspartic monolayer poly(amideid 3-benzoyl pyridine) and the suggested chemical structure.

3.3.3. NMR Spectroscopy

The resulting pyrrole polymers were characterized by several techniques. As the material is not highly studied, it was possible to obtain NMR spectra of the polymer. The ^1H -NMR spectrum of the obtained polymer is in good agreement with the proposed structure as depicted in Figure 3-21. It shows one peak at 7.20ppm, which can be attributed to the proton in the 4 position of the pyrrole moiety. This indicates that the polymer formed is very highly 2,5 linked. The NMR also clearly shows signals due to the alkyl chain of the substituent. How strongly the resonance frequency of the aromatic proton is shifted depends on the degree of oxidation of the polymer backbone. If there were any other oxidized product or remaining monomers, there were only minor amount since the NMR does not indicate any additional compounds other than the 2,5 linked polypyrrole. There were no signals due to an end group being visible.

3.3.4. Gel Permeation Chromatography

Polypyrrole products under various conditions were also analyzed by GPC. The UV-detection revealed two peaks for the polypyrrole (product) one corresponding to monomer and the other corresponding to polymer with a polystyrene equivalent molecular weight range (M_w) of approximately 2,000 to 6,000. Figure 3-22 shows the pressure dependence on its molecular weight with different mole fractions of BDDP. According to the results, it is clear that with an increase in surface pressure, the molecular weight has been increased. This could be due to the resistance of the molecule. If the molecule is oriented 2.5 pyrrole position with adjacent molecules, polymerization will

take place with much ease. Another observation is molecular weight increases with increase in NODP and maximum M_w was at the 50% mixture of THDP and NODP. This is also could be attribute to the orientation of the molecules in the mixtures. The measured molecular weight depended on how long the sample was exposed to air on the rough surface or in THP solution. The M_w of the polymer from 3-thiophenyl pyrrole was also slightly higher than that for the benzothienyl analog.¹⁷ However, the polypyrrole calibration curve is perhaps a poor standard for the materials investigated as the polypyrrole backbone suffers considerably at higher degrees of oxidation. The measured molecular weight only shows that polymer is formed.

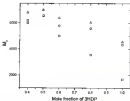


Figure 2.12. GPC data of different composition of THDP and NODP. \blacktriangle = M_n , \square = M_w .

2.7 Conclusion

We were able to prepare stable monomolecular layers of mixtures of HEDP and HODP with thickness of 2%–30%. HODP was thought stable polymer films could not be made of 100% H-oxide/yl particles. The monomers were polymerized as LiB-films on aqueous solutions containing an oxidizing agent. By recording the thickness of the monomer mixtures and copolymers, we found that the copolymer films appeared to be more stable than the LiB-films of the monomer mixtures. GPC data confirm the copolymerization. IR and NMR results indicate incorporation of the polymers and suggest that the HODP units a more easily able to incorporation than the H-alkylated derivatives.

CHAPTER 3 MASS SPECTROMETRY OF POLYMERIC MATERIALS

3.1. Introduction

Mass spectrometry has become a valuable technique for characterization of synthetic polymers, especially low molecular weight polymers. The popularity of this method increased because of its quickness and the accuracy of determining the absolute molecular weight distribution compared to classical techniques of polymer analysis. Moreover, data on the nature of repeat units, polymer additives, impurities, and structural information can be obtained. Low volatility and thermal lability have set an upper mass limit of detection, but this problem has been overcome by using a variety of soft ionization techniques such as matrix-assisted laser desorption/ionization (MALDI). Analysis of molecular weights, molecular weight distributions, end-group structure and end-group modifications of wide range of synthetic polymers were done employing MALDI-MS.^(1,2,3) Controlled MS/MS fragmentation of copolymers (sequencing) important in order to establish the type of copolymer (block, random, alternating), the position of the blocks, and the block length distribution. It is apparent that a lot of work still has to be done in this area since there are very few data found in literature. Statistical modeling of the mass spectral structures of copolymers has been used to investigate the microstructure of the polymer.^(4,5,6) Recent investigations of IR absorbing moieties^(7,8,9) legal modification to facilitate the use of lipid moieties,⁽¹⁰⁾ and

lyzed of LCMAALCM (50/50) ^(16,17) open new avenues get information from high molecular weight materials.

The major goal of the mass spectrometry project of this dissertation is to obtain sequence information of a copolymer produced from two different monomers (polymerization in a solution and in a Langmuir film). Since these monomers monomers (3-benzothienyl pyridine and N-benzothienyl pyridine) are related to a specific very at the material interface, the reactivity of monomers is restricted. Thus, the reactivity of these monomers should be different from the solution polymerization, which would ultimately alter the sequence of the copolymer. Studying the sequence with different polymerization conditions, one could investigate the reactivity of these monomers relative to the specific polymerization surroundings. Unfortunately, we have not been successful in this in obtaining the sequence of the copolymer. However, the initial data, which have been obtained towards pursuing the final goal of this research, is discussed in this chapter.

3.2 Experimental Procedures

Monomer samples were sublimated in the Mass Spectrometry Laboratory (MS lab) in the Chemistry Department after purification, but the polymer samples were made according to Section 3.2.1.7 and then sublimated to the MS lab.

3.2.1 MALDI-TOF Experiments

Analysis molecules are embedded in a small, highly absorbing organic compound which induces an efficient transfer of the laser pulse energy to the analyte as well as a soft desorption process.⁴² In the present case species of all polymers investigated, cation attached molecular ions of the embedded-analytic molecules were exclusively observed.

3.2.1.1 Sample preparation

Three matrices (DMB, DTL, and MABA) (Figure 1-6) were tested with the polymer material obtained from Langmuir method. The analyte and the DTL matrix gave us best results and only those are here discussed later. Samples were prepared for the MALDI experiments in the following way. First, 1-10 mg/mL of 1,4,5-substituted (DTL) was dissolved in the solvent mixture of CH₂Cl₂/CH₂Br-Ethyl Acetate (3:1:1). The samples were dissolved in LC grade Chloroform in a concentration of 5 mg/mL. 0.5 μ L of analyte solution was mixed on the target with 1 μ L of matrix solution and dried in a gentle stream of air.

3.2.1.2 Mass spectrometry

Initial experiments were done employing the MALDI-TOF technique using the Vision Laserdes unit (with a light tube of 1.2m), which was run by Mass Spectrometry Services in the Chemistry Department. Some of the MALDI results were reproduced using a Finnigan LASSERMAX (with light tube of 0.5m) which was in Dr. B. Fritsch's Lab.

a)



2,4-dihydroxybenzoic acid (DHB), MW = 154.03

b)



1,2,3-trihydroxynaphthalene (OFL), MW = 204.20

c)



2-(4-hydroxyphenyl)-5-oxopentanoic acid (HABA), MW = 240.23

Figure 3.1 Structure of MALDI matrices used in this study: a) DHB, b) OFL, and c) HABA.

Each sample had an M_0 laser source with a wavelength of 337nm. All of the spectra were obtained in the positive ion mode. The laser pulse energy varied from sample to sample, but the acceleration voltage was kept constant at 30kV. The final mass spectrum obtained was an average of 10-15 individual scans.

In order to calculate the average molecular weights of the polymers, the following method was used. First, a certain sequence of peaks was chosen (e.g. $Si-H_2-M_0$, $Si-M_0$, or $Y-M_0$, see Table 3.1). Then, the area under the peak was integrated after drawing a baseline between the adjacent peak valleys. The integrated peak areas, reflecting the number of ions (N_i) were used with corresponding m/z values to calculate the number average (\overline{M}_n) and weight average (\overline{M}_w) using the following equations:

$$\overline{M}_n = \frac{\sum N_i M_i}{\sum N_i} \quad (3.1)$$

$$\overline{M}_w = \frac{\sum N_i M_i^2}{\sum N_i M_i} \quad (3.2)$$

$$polydispersity = \overline{M}_w / \overline{M}_n \quad (3.3)$$

It is important to mention that many experimental parameters give rise to mass discrimination in the signal generated from a mass spectral analysis of polydisperse polymers. The mass bias can be introduced from sample preparation and desorption/ionization process. Analysis also assumes that the sensitivity of the detector is independent of the mass range of the ions detected. Therefore the average molecular weights that calculated in this text are an estimate value and indicative of polymer distribution.

3.2.2 GC-MS Experiments

In this subchapter, two different ionization processes, electrospray (ESI) and atmospheric pressure chemical ionization (APCI), were explored, but only APCI produced promising results. Only results obtained from APCI are discussed here.

3.2.2.1 Sample preparation

A very small amount ($\sim 0.2\text{mg}$) of the sample was dissolved in $100\mu\text{L}$ of THF in a polypropylene microcentrifuge vial.

3.2.2.2 Mass spectrometry

Sample ionization was done by using a syringe pump flow injection analysis, where the flow rate was $20\mu\text{L}/\text{min}$ of THF and the injection loop was $5\mu\text{L}$. The ESI/CI was carried out using an Applied Biosystems, Model 400, solvent delivery system. The separation of the polycyclic material was carried out using two columns ($300 \times 7.5\text{mm}$) with Phenomenex, Phenogel 5\AA and 300\AA . When the polycyclic materials were investigated, the sample was introduced to the APCI source via flow injection analysis, i.e., use of an ESI injector with a $5\mu\text{L}$ loop but no column. The split ratio was 75% to the source and 25% to the waste. The mobile phase (THF) was run for 15 minutes to prepare

the column before injection. There was an UV-Detector ($\lambda = 214\text{nm}$)/Applied Biosystems, Model 780 in line between column and split and APC2.

A Finnigan MAT LQ4 ion-trap mass spectrometer fitted with an APC2 source was used to acquire data in the positive ion mode. A capillary temperature of 250°C and a vaporizer temperature of 600°C were used with a sheath gas flow rate of $30\text{ }\mu\text{L/min}$ and an auxiliary gas flow was zero. The discharge current was $5\text{ }\mu\text{A}$. The mass spectrum was obtained by averaging data sets with desired retention times from the chromatogram.

3.1. Results and Discussion

3.1.1. MALDI-TOF/MS

The monomers and the polymers were tested with several different matrices and solvent systems. Most of the results with polymer were unsuccessful, the main problem being the inability to incorporate the analyte into the matrix. When the matrix (mixed with the analyte) was slowly dried, the analyte phase separated and was not incorporated into the matrix crystals. Different solvent mixtures were tested to control the evaporation. The best results were achieved when the $\text{CH}_2\text{Cl}_2/\text{THF}/\text{Et}_3\text{N}$ (5:5:1) solvent system was used. Also, a list of MALDI matrices investigated is shown in Figure 3-1. After several combinations of solvents and matrices were used, the best results were obtained from the DTL matrix with the above solvent system.

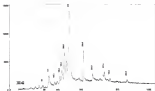


Figure 3.2 MALDI spectrum of DTL matrix

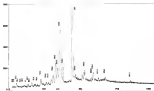


Figure 3.3 MALDI Spectrum of HOOP in DTL matrix

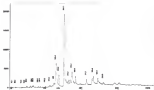


Figure 3-4 MALDI Spectrum of NCOF in DTL matrix

First, the DTL matrix which was dissolved in THF and TOF mass spectrum was investigated to observe the predominant ions produced (see Figure 3-2). The most abundant peak corresponded to the $(M+H)^+$ ion, m/z 125. The peak positions were shifted to the lower mass range by 366 units. There were lower intensity peaks at m/z 103, 181, 211, and 231 for the $(M+H-CH_2)^+$ ion, $(M+H-2OCH_2)^+$ ion, $(M+H-NCH_2)^+$ ion, and $(M+Ag)^+$ ion, respectively.

Figure 3-5 shows the MALDI spectrum obtained from monomer of NCOF in DTL matrix. The peak positions shifted to the lower mass range by 366 units. In the mass spectrum, m/z 176, 184, 208, and 228 peaks corresponded to the DTL matrix (These peaks match Figure 3-2.) The peak m/z 140 related to the $(M+H-CH_2)^+$ ion. The

most abundant peak, m/z 371, is from the HODP $[M+H]^+$ ion. Any fragmentation of the HODP is not apparent. In Figure 3-4, we observe the MALDI spectrum of HEDP in DTL matrix. The peak positions were shifted to the lower mass range by 2m/z units. The $[M+H]^+$ ion of HEDP was at the m/z 298 position. The matrix-associated peaks are still 285, 325, and 345. The HEDP was not subjected to fragmentation due to the ionization process used here.

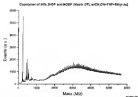


Figure 3-3 MALDI-TOF spectra of 50% HEDP and HODP copolymer with matrix. DTL is $CH_3CN/THF(40/60)$, Ag^+/Na^+ .

Then, a copolymer with a 50% mixture of HEDP and HODP was investigated (Figure 3-5) using MALDI and DTL as the matrix. The matrix used in this sample was obtained in $CH_3CN/THF(40/60)$, Ag^+/Na^+ , and the peaks obtained from the data are shown in Table 3-4. The mixture of solvents was used for two reasons (1) to get the analyte

thoroughly mixed with the matrix and (2) to control the evaporation, leaving behind an embedded analyte in the matrix. Spiking the matrix monomer with ^{15}N helped the verification process of the analyte. According to the data shown, 50% copolymer had molecular weight distribution ranges from 1200-4000 Da (approx. 5-10 repeats) and the proves that polymer was formed. Also, the copolymerization data contained sequences corresponding to the mass of each monomer (289's for HEDP and 311's for HODP) and those of the dimer copolymer pairs (600's). By having sequences of corresponding sequence units, this data shows that both monomers were chemically incorporated. According to the mass spectrometry data, $\overline{M}_n = 341.8\text{Da}$, $\overline{M}_w = 354.1\text{Da}$, and polydispersity = 1.039 were calculated (as described in section 3.2.1.2) using the data points from $m/z = 1380$ to 5700. Since the higher molecular weight materials have a low volatility, these values obtained from the mass spectrum are only an estimate.

The homopolymer of HEDP was analyzed using the same matrix (dibromodifluoromethane) and the molecular weight distribution ranges from 1800-4800 Da (approx. 8-16 repeats). According to the mass spectrometry data (Figure 4-6 and Table 3-2), $\overline{M}_n = 204.8$, $\overline{M}_w = 218.7$, and polydispersity = 1.069 were calculated. These values obtained from the mass spectrum are not only an estimate since the volatility of higher molecular weight is low.

Even though sequence information can be extracted using the MALDI-TOF data, we did not have the resolution needed to completely separate out the peaks. The main reason for multiple peaks may have been the polymerization method (solution coupling) used here, which produced many macromolecules of different level of cross-linkages (probably). For instance, a series of peaks correspond to monomer with a hydroxyl group

attached were observed (peak difference of 360). According to the data, a polymeric material incorporated with side products were formed here.

Table 3-1 Peak positions and the peak assignments of some selected peaks of the MALDI-TOF spectra in Figure 3-6. A = 2H2OP, B = 7H2OP, X and Y = unknown.

Peak Position	Peak assignment (calculated)
1182	3(A-B)+76 ⁺ [1182]
1192	X [1192]
1202	Y [1202]
1118	X+A [1118]
1254	Y+B [1254]
1400	4(A-B)+76 ⁺ [1400]
1409	X+5A [1409]
1546	Y+2B [1546]
1711	X+5A [1711]
1874	Y+3B [1874]
2020	3(A-B)+76 ⁺ , X+4A [2020]
2136	Y+4B [2136]
2240	X+5A [2240]
2312	Y+5B [2312]
2550	X+5A [2550]
2636	4(A-B)+76 ⁺ [2636]
2870	Y+5B [2870]
2954	X+5A [2954]
4147	Y+7B [4147]
4202	X+5A [4202]
4240	3(A-B)+76 ⁺ [4240]
4400	Y+7B [4400]
4492	X+5A [4492]
4774	Y+8B [4774]
4922	X+5A [4922]
4971	5(A-B)+76 ⁺ [4971]
5074	X+5A [5074]
5291	Y+8B [5291]
5362	X+5A [5362]

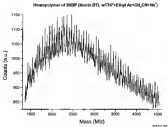


Figure S-4 MALDI-TOF spectra of BBDP homopolymer with matrix DPL, in CH₂Cl₂/THF/EtOAc Ac=20.

In order to have a better understanding of the polymeric products, we turn to ion Trap-mass spectrometry. Our goal was to isolate a desired peak, dissociate it using CID, and observe the daughter species. Initially, we wanted to know how much energy was needed to automate the experiment and what the fragments were.

Table 3.2. Peak positions and the peak assignments of some selected peaks of the MALDI-TOF spectra in Figure 3-1. X = DEP, Y and T = unknown

Peak Position	Peak assignment (calculated)
1466	X+Na ⁺ [1466]
1566	X [1566]
1628	T [1628]
1753	X+Na ⁺ [1753]
1858	X+X [1858]
1926	Y+X [1926]
2083	X+Na ⁺ [2083]
2173	X+Na [2173]
2258	Y+Na [2258]
2358	X+Na ⁺ [2358]
2427	X+Na [2427]
2573	Y+Na [2573]
2626	X+Na ⁺ [2626]
2738	X+X [2738]
2814	Y+Na [2814]
2914	X+Na ⁺ [2914]
3040	X+Na [3040]
3128	T+Na [3128]
3233	X+Na [3233]
3294	T+Na [3294]
3427	X+Na [3427]
3444	T+Na [3444]
3512	X+Na [3512]
4200	X+Na [4200]
4241	T+Na [4241]

3.3 LC-APCI-MS

Figure 3-2 shows the fragments of monomers DEP and NDEP. The connection method used here was Atmospheric Pressure Chemical Ionization (APCI), which is well

known to give preferentially single charge ions. The measured MSDF showed less fragmentation than MSDF when CID energy of ~20% (max. 10V) is applied.

Fragmentations of these monomers were taking place along the chain with specific fragmentations shown in Figure 3-8. When a partially oxidized monomer of BSEP (MW 306.3) was isolated and fragmented, most of the fragments came from the long chain, but one fragment opened the pyridine ring (Figure 3-9). The dimer of BSEP also was isolated and dissociated using CID. Dehydration and cleaving the C₁₂ end of the C₁₂ chain was observed (Figure 3-10). A major disappointment was that we were not able to cleave the bond between the pyridine ring to isolate the monomer units which would shed some light on the structure of the polymer. Our goal was to break the bonds between the pyridine rings, but with no fragmentation along the alkyl chain. The applied CID-energy is expected, because we could obtain the maximum amount of energy that could apply on the molecule without fragmenting along the long alkyl chain. But something in the results, the energy required to cleave the bonds along the alkyl chain were smaller than the energy needed for breaking the bond between the pyridine ring.

One major problem of the mass spectrum analysis of these samples was the separation of the low molecular weight substances that were saturating the mass spectrum. These spectrum were flooded with noise and did not show any peak separation. After using a C₁₈ column attached to the HPLC, we were able to separate the samples according to the size and beneficial for obtaining better mass spectrum. These spectrum had clusters of peaks which were separations of monomer units (Figure 3-11). The results obtained without the C₁₈ column are not shown here. Unfortunately our HPLC gradient was ended at this point.

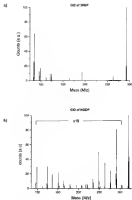
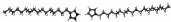


Figure S-7 Densities spectra of monomers after CID: a) HCOF, b) HCOF



(a)

(b)

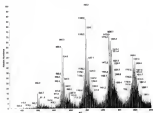
Figure 1-4 Representation of monomers (a) 3EDF (b) 3ODF



Figure 1-5 Representation of partially oxidized 3EDF monomer



Figure 3-10 Fragmentations of the Anion of THF



3.4.....Conclusions

MALDI-TOF results indicated that polymerization had taken place as both with the HEDP alone and mixture of HEDP/HODP. In the copolymer, the AB-dimer sequence were clearly present ($A = \text{HEDP}$ and $B = \text{HODP}$). There were also 10-12 repeat-of HEDP and HODP alone were observed in the copolymer mixture (Table 3-1). This indicates that copolymer of HEDP and HODP is a random polymer. According to the MALDI-TOF results, there is an increase in molecular weight in the copolymer of HEDP/HODP compares to the homopolymer of HEDP obtained from the Langmuir method.

The main problem in the MALDI analysis of the synthetic polymers, which is still in the existence, is the search for optimal matrices. A good solubility of matrix and polymer in a common solvent is the prerequisite for a good matrix. Most of the matrices are polar substances which work well with low polymers but less effective with synthetic complex materials. The ideal matrix should perform both essential steps in MALDI, desorption and the ionization of the synthetic polymer. In both homopolymer of HEDP and copolymer of HEDP and HODP, matrix DTL gave the best results, but a better matrix should be found to obtain more reproducible results.

Since oxidative polymerization produces oligomers with different degrees of oxidation states, there are many different products at the end of the polymerization. As seen in many mass spectra, there are many low molecular weight products that broad the spectra that we were not able to see in the higher molecular weight polymer products.

After using an online SEC column, separation was obvious, and better than spectrum was observed.

CHAPTER 4 X-RAY DIFFRACTION OF LANGMUIR AND LANGMUIR-BLODGETT FILMS

5.1 Introduction

X-ray diffraction gives extraordinary insight into the material in the monolayer state in that structural order of the substance can be determined. In this chapter, three different experiments were conducted in order to gain an understanding of the behavior of BDDP and NDDP in their bulk states, Langmuir film state, and Langmuir-Blodgett film state. Initially, the monomers of BDDP and NDDP were characterized using powder diffraction. Next, transferred films (Langmuir-Blodgett films) of monomer cations with different compositions were investigated. Both of the above-mentioned experiments were done at the Butler Polymer Laboratories, University of Florida, using a tube source X-ray diffractometer. The final characterization of the materials was done employing grazing incidence X-ray diffraction (GIXD) on Langmuir monolayers. Initial characterizations were performed at the National Synchrotron Light Source, Brookhaven National Laboratories, Upton, New York, and at the Advanced Photon Source, Argonne National Laboratories, Chicago, Illinois. The primary goal of X-ray studies was to understand the amphiphilic materials used in their bulk state and structural order in Langmuir and Langmuir-Blodgett films. Better understanding would lead to better control of these and similar Langmuir films to achieve desired physical and electronic properties, which could be manipulated to optimize as LEP applications.

4.2 Experimental Procedure

Powder diffractions of TiO_2 , NiO , and the fractured film was done with a Bruker AXS platformTM instrument (Figure 4-1), which contains a 3-axis goniometer in which θ was the rotation of the sample, 2θ is the rotation of the sample including the γ circle assembly, and 2ψ is the axis which the detector is rotated. Figure 4-1 shows that γ can be moved manually to 5° (see picture) or 90° (see schematic) angles.



Rotation axis of Sample



Figure 4-1 Bruker AXS PlatformTM instrument and a schematic of rotation axis of the sample

The diffraction system included a Kristalloflex 7000 X-ray generator with a standard Cu tube source. Copper anodes were used as source monochromators Cu ($K_{\alpha 1} = 1.5405 \text{ \AA}$) X-ray radiation, which was collimated using graphite collimator (apertures of diameter 300 μm in the back and 50 μm in the front). The distance between the sample and the detector was 60 mm. The detector, (Si-PTLRTM), was a P20012 multi-wire, gas-filled

scat-detector. The diameter of the detector and the intensity were corrected by oversampling (using an image obtained from uniform X-ray source of Fe^{2+}) the image, and the detector position was calibrated using a ceriumium (Ce_2O_3) powder sample. The software used in this setup was GADDS (General Area Detector Diffraction System) which was able to display a real-time image of the diffraction pattern. The GADDS software was designed to do texture analysis, polymer diffraction, powder diffraction, small angle scattering, and amorphous scattering. The software was controlled all the parameters from the computer.

4.2.1 Powder Diffraction of Monomers of BDDP and MDDP

The X-ray diffraction of the sample was performed in the transmission geometry. The powdered sample was packed into the 1 mm diameter thin wall glass capillary tubes and sealed by flame. Then, the glass capillary was mounted in the sample holder using wax. The sample was rotated in $\omega = -30^\circ$, radius of the rotation goniometer head screen was adjusted until the sample was positioned at the focus of a fixed oilysing optical microscope. This keeps the source-to-sample distance constant and also at the center of the goniometer. The sample is then taken back to $\omega = 0^\circ$ and the software control changed to the record mode. While looking at the glass capillary through the optical microscope, the sample was rotated in ϕ axis to observe for any reflections of the sample. The screen at the goniometer head were adjusted to maximize the widthness. When this was accomplished, the X-ray generator was set to 50kV and closed, and the data were collected for 15 hrs in the rotate frame mode. In this rotate frame mode, the ϕ

axis is rotated at a speed of $1^\circ/\text{s}$, while α and 2θ are kept stationary and the ϕ axis was kept at 100° .

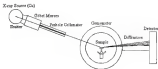


Figure 4-2 Schematic of the Reflection Geometry

4.2.2 X-ray Reflection of Lamellar-Block Copolymer

First, the sample (LB film on a solid substrate) was not dried vacuum desiccator. Then, it was cut into a 2 cm X 2 cm square, which was mounted on the sample holder with double-sided tape. The X-ray diffraction of the sample was done in reflection geometry (Figure 4-2). At this time, the beam-stop was removed, and the X-ray generator was set to 20 kV and 15 mA. The direct beam was collected for 3 seconds, and the beam intensity (I_0) was measured. In order to align the sample, it was positioned so as to block half of the beam intensity (I_0). When approximately $1/2 I_0$ was obtained, the sample was rotated 180° in the ϕ direction. The objective was to get the same amount of intensity

(approx. $1\mu\text{m}$) when the sample was at $\theta = 0^\circ$ and 180° . This was achieved by adjusting a screw on the goniometer head. When adjustment was accomplished, the beam-stop was attached, the X-ray generator was set to 30kV and 80mA, and data were collected for 5 hrs in a single-scan mode. In a single-scan mode, one of the dimensions (i.e., x or 2θ) can be set to scan for an angle or a set amount of time. The scan was done linearly $= 0^\circ$ to 1° in 5 hrs. After the data collection was done, the two-dimensional image was averaged and integrated in the y direction in order to get a graph of 2θ vs. intensity. The d -spacing of the molecules can be calculated from the peak position using the Bragg equation

$$n\lambda = 2d\sin\theta$$

1.2.3. X-ray Diffraction of Langmuir Films at Air/Water Interface

Dr. Doran's group had collaborated with Dr. Paula Goffin's Group at Northwestern University (NWU), regarding the X-ray Diffraction of the Langmuir films. Recently, we (Dr. S.B. Doran's) group built our own setup at Michigan Research Collaborative Access Team (MRCAT),^[10] Advanced Photon Source (APS),^[11] at the Argonne National Laboratories.^[12] Even though I have spent my final two years of graduate school designing and building the complete setup, we have been able to get only very preliminary data. Therefore, I will discuss the NWU setup here, but I will include our newly-built setup in chapter 2, emphasizing the flexibility and the user-friendliness of our setup. After commissioning our setup at MRCAT, it will be a vital tool for our research group to be able to obtain structural details of Langmuir films. The

experimental procedure for this part had to be very detailed since it was expected for our group to get rewarded on this field.

4.2.3.1 Differential apparatus

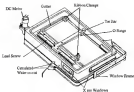


Figure 4-3 Sketch of mechatronic body ^[4]

A Langmuir trough used in this experiment was designed and built by Barbara

Low,¹⁴⁰ and later modified by Mingzhu Shih.¹⁴¹ The following is a description and

Figures are extracted from Mary Barber's Ph.D. dissertation.¹⁴² A schematic of the setup

is shown in Figure 4-3 and Figure 4-4. The trough was coated from Aluminum, which

provided rigidity and good thermal protection for temperature control. All the parts of

the trough which came in contact with either the monolayer or the pure water subphase

was coated with Teflon, a chemical-resistant polymer, and a hydrophobic surface

similar to Teflon. The handle was made out of teflon tape. The trough had dimensions

of 11" x 6" x 0.25"

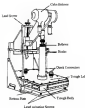


Figure 4-4 Schematic diagram of monolayer trough used for X-ray diffraction experiments.¹⁴³

with channels just beneath the water sealed surface, which helped to maintain the temperature of the electrolyte at $\pm 1^{\circ}\text{C}$. The temperature was measured using a platinum Resistance Temperature Detector (RTD) which was inserted into the channels/body of the trough. The top half of the trough had a separate water circulation, which maintained a temperature of approximately 2°C above the set temperature of the trough so that condensation on the windows was prevented. Also, the fill helped with thermal isolation, protection against corrosion, and contamination.



(A)



(B)

Figure 4-1 Specimen X-ray diffraction setup. (A) Inside of the trough (balance beam and the furnace are visible), (B) Outside of the trough (Channel, D-I, in slight contact with the window).

The trough was designed to be airtight so that it maintained the monochromator atmosphere during an observation. Also, it helped to maintain a slightly positive Helicon pressure in order to maintain the reduction damage and the air monitoring of X-rays. A silicon/bismuth melt-out of Thelma controlled the profiled area of the monochromator (Figure 4-3). The heater movement in this setup accommodated approximately 15in^2 to 1.5in^2 , a

[1] **samplement table** The effluent barrier extended above the water surface allowing the monolayer to be compressed, but there was a gap between the bottom (flexo-actuated) surface and the barrier that allowed the water to flow beneath it. The motion of the barrier was accomplished by having a 10" travel square wave transducer coupled to a DC motor. X-rays entered/well exited the system through a long slit cut into the trough body. The slit was covered with 12µm Kapton film.

Figure S4 displays a schematic diagram of the NWFI setup. The X-ray beam, both was at an upward angle and horizontally defined by a slit, S-1. Using the mirror, M, the beam was deflected downward in the sample at an angle of ~ 1 degree. The incident beam on the sample was collimated through a slit, S-2, with a vertical height of 200µm and a width of 1 mm. Slit S-2 also helped to reduce the parasitic scattering. The Detectors, D-1, helped monitor the beam and its status that beam was present after the slit, S-2. Since so many parameters were involved in Synchrotron X-ray beamline and in our setup, monitoring the beam in several different positions gave us updates on the status of the propagating beam at real-time, especially when modes were poor. Since the fluctuation of the intensity of the synchrotron beam was substantial, detector, D-1, was used to monitor the signal obtained by the detector, D-3. Also the detector, D-3, dropped its intensity when the water level of the trough was lowered, which we also continued to monitor. The slit, S-4, blocked the incident beam from the mirror, M, and accepted only the reflection from the water surface to be monitored by D-3. All three- D-1, D-2, and D-3-are NaI scintillation Detectors and were purchased from Canberra®. In some instances the detectors were covered with the signal and several layers of aluminum foil were attached to the front of the detector to attenuate the beam. Any X-

ray scattered by the sample was detected by (D-2), which can be rotated azimuthally about the sample by a Motor 1-circle goniometer. Two sets of Soller slits were at the S-2 position to define the detected scattering from the sample. The angular acceptance of

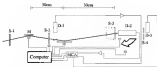


Figure 4-4 Schematic of the Synchrotron X-ray Diffraction setup

the horizontal and the vertical Soller slit were 3.4mm and 10mm, respectively. Further discussion of Soller slit and angular acceptance can be found in chapter 5. The amplified output from the D-1 and D-2 were fed simultaneously into a computerized multichannel analyzer. The trough was kept on a top of a Newport vibration isolation table to minimize effects from the experimental floor vibrations.

The nuclear process (β) was measured by the Millikan plate method using a sealed Cs-137 source/insulator and filter paper plate. The plate hung through a hole in the trough cover, and a telescoping shield around the hanging wire insulated the balance and the trough wall kept the entire system grounded. The balance was on a separate

vertical slide, which was adjustable to lower the plate gradually into the water surface.

The position of the measurement of D was 40 Lath/m.

Closing the trough, selected preparations, spreading the monolayer, and all other regular Langmuir monolayer procedures were followed, as explained in Section 3.2.1. After the trough was cleaned, the lid was closed, and Wilhelmy plate was lowered. After both the balance and the temperature were stabilized, the monolayer was spread through a reasonable hole in the cover and kept in Italian pumps for 5 min before compressing the monolayer to the desired surface.

Experimental data that have been discussed here were obtained at the Oak Ridge National Laboratory beamline (X-34A)¹⁴⁰ of the Synchrotron Light Source,¹⁴¹ Brookhaven National Laboratory.¹⁴² The X-ray beam was focused in a vertical direction and was deflected upwards by 0.5° and. The X-ray energy was fixed at 8.04 keV. In order to minimize the scattering from the water, the angle of incidence to the interface was kept below the critical angle for total external reflection of the X-rays.¹⁴³

3.2.1.2. Alignment

The apparatus here was leveled first, and the center of the deflecting mirror and the center of the Huber were fixed up along the beam path. After taping two photoconductive papers on the front and the back of the hatch, a string was stretched between the centers of the images to obtain the beam path.

Next, the deflecting mirror angle was set. In order to find an upward deflection of the beam from the monolayer surface, the following procedures were followed. Two Diqu

vertical slit spaced 4 cm apart, was adjusted in height to allow the beams to pass through both with maximum intensity as measured with ionization chambers. The heights of the slits were measured, and knowing the distance between them, the angle of spread (deflection) of the mono-chromator was calculated. Since the spread angle was known, the mirror was adjusted to deflect the beam (downward) to the desired angle of 1.265° (small). In order to minimize the scattering from the water, the angle of incidence to the interface was kept below the critical angle for total external reflection of the X rays (2.64 mrad for 60 keV energy).

The sample slit, S-2, was spaced to a height of 200 μ m and was set to allow only the reflected beam from the mirror, M. Any of the incident beams on the mirror, M, which passed underneath it was blocked by slit, S-2. The size of the scattered angle was roughly assigned by observing the maximum intensity of the detector, (D-2) (but an ionization chamber was used instead of a scintillation detector) since the scattered angle varied.

A photofluor card was mounted on the back of the wall of the experiment tank to observe the reflected beam from the water on the trough. When the trough height was changed, the reflected beam from the water would change in intensity. Trough height was adjusted to the maximum reflected beam position. While the reflected X ray beam from the sample (water) was measured by the detector, D-1, the slit, S-4, blocked any incident beam from the deflection mirror, M. The system was considered aligned at the moment, and more precise calibration of the scattered angle was performed later.

Silica powder was sprinkled onto a double-sided tape, which was attached to cardboard. The cardboard was placed in the center of the paracasser in the reflection

mode, and the Si (111) peak was observed. The peak maximum was set to $K_{\alpha} = 1.005 \text{ \AA}^{-1}$.¹ Then, Si(110) was observed at $K_{\alpha} = 1.072 \text{ \AA}^{-1}$ to double-check the angles. In order to ensure the calibration and the technique, normally a standard monolayer, 1-hexadecanethiol ($\text{C}_{16}\text{H}_{33}\text{SOH}$), was run at pH = 2 and at 30°C. If the expected peaks, 1.005 \AA^{-1} and 1.08 \AA^{-1} , were observed at $2\theta = 2\text{Kost}(\alpha)^2$ then the final calibration was done, and the apparatus was ready for use from unknown monolayer samples.

4.1 Results and Discussion

4.1.1 Powder Diffraction of the Monomer

Powder diffraction of the monomer was done as explained Section 4.2.1. The powder diffracted pattern of MOP is shown in the Figure 4-1a. The raw data (i.e. was unscattered first and then integrated over 2θ , and the data are shown in the Figure 4-7b). Since the molecule contains a long alkyl chain and a polar head group, a lamellar structure was expected, and a calculation was done to investigate order in the bulk. The d -spacing of the corresponding peak was found and treated as shown in Table 4-1. The d -spacing of the lamellar was calculated as 46.97 \AA , and standard deviation was 2.8 \AA . The powder diffraction of MOP also was done, the raw data are shown in Figure 4-8a, and the integrated data are shown in Figure 4-8b. Even though the peak maximum and the positions are different, peaks showed character was similar to the MOP diffraction pattern. MOP is also expected to pack in lamellar fashion, and calculated values are shown in Table 4-2. The d -spacing of the lamellar was calculated to be 34.18 \AA , and the standard deviation is 1.28 \AA .

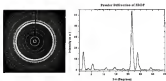


Figure 4-7 Powder diffraction pattern of 2H2P (left) Diffraction-image (right) Graph of the data, Intensity versus 2θ

Table 4-1 Data obtained from the powder diffraction of 2H2P

hkl	2 θ (Degree)	d-spacing (\AA)	$I \times d$ (\AA)
001	1.79	49.91	49.13
002	3.60	24.94	49.09
003	5.45	16.63	49.05
004	11.90	8.04	49.26
006	14.45	6.11	49.04
2010	18.90	4.93	49.19
110+110	21.71	4.09	N/A
101	21.79	3.98	N/A
2014	26.10	3.43	49.19

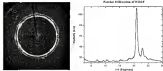


Figure 4-8 Powder diffraction pattern of MCDP (left: Diffraction image; right: Graph of the data, Intensity versus 2θ)

Table 4-2 Data obtained from the powder diffraction of MCDP

2θ	d -value (Degree)	d -spacing (\AA)	$h^2 + k^2 + l^2$
004	9.57	9.15	24.9
007	11.83	7.52	36.1
0010	13.99	6.46	44.4
0011	16.37	5.45	55.1
110-110	21.48	4.14	N/A
080	23.31	3.82	N/A
0018	28.91	3.14	64.9

The two-dimensional packing of alkyl chains was seen in the 2θ range of 21 – 24° .

These d -spacing values (4.09 , 3.75 \AA and 4.14 , 3.81 \AA , respectively for MCDP and MCDP)

are very close to the d spacing values of $1T_1$ 3.34 Å for $\{110\}+\{1\overline{1}0\}$ and $\{001\}$ observed for the $C_{60}/SiO_2/CXCR$ as air/water interface.

4.3.1. Grazing Incident X-ray Diffraction Of The Langmuir-Blodgett Films

The Langmuir-Blodgett films were prepared as explained in Section 3.2.1. X-ray diffraction was done within 24 hrs of the sample preparation. The minimum required surface pressure for transfer was found to be above 33mN/m. Best results were obtained with 50 to 60mN/m. The transfer speed of about 1 to 3×10^{-2} cm/min² (around $\frac{1}{2}$) and the dipper speed of about 10mm/min were optimum and were kept constant for all the compounds. Scattering suggested that 50% and 60% monolayers of both HEDP and NEDP pack better on the air/water interface than HEDP alone.

The quality of the film was measured by the transfer ratio (T_r) parameter, which is described in equation 3.7. The samples which had T_r values higher than 0.50 were chosen for X-ray diffraction. Figure 4-9 shows a detector image of the diffraction.



Figure 4-9 Diffraction image of 40 nm-thin layer NEDP LB-film

obtained from the 100% 3EDP monomer sample with 43 multilayers. The first peak in Figure 4-5 is due to the total reflection of the substrate. All peaks are observed along $\chi = 0$ since periodicity of the layers is normal to the substrate. In order to investigate the influence of NEDP, another two samples—60% 3EDP/40% NEDP, and 60%3EDP/40% NEDP Langmuir-Blodgett films with 46 and 39 multilayers—were used in the X-ray diffraction experiments. All three samples were run for 2 hrs in two different sample areas to see the effects on the sampling area.

The data obtained from both exposures of the same sample were given the same peak positions. The peak positions and d -spacing information are illustrated in Figure 4-11 and in Table 4-3. The first peak is approximately at $2\theta = 8.6^\circ$ is due to the total reflection of the substrate. The first order peak from the LB film is observed at $2\theta = 2.8^\circ$ for all three samples. The d -spacing of the three samples was obtained by calculating the average of three peaks observed. The d -spacing are 49.4Å, 49.1Å, and 50.4Å for 100% 3EDP, 60% 3EDP, and 40% NEDP, respectively. The substrate the samples were Y-type Langmuir-Blodgett films (see Figure 1-3). The calculated bilayer average distances for fully extended (as 100% with staggered conformation (Figure 4-8b)) were 49.5Å, 50.5Å, and 51.6Å for 100%-to 60% of the 3EDP samples. Since the calculated distances were very close to the observed values, it suggests that Langmuir-Blodgett multilayers may be somewhat tightly packed with maximum or no tilt in the long alkyl chain with respect to the substrate. Also, the intensity drop in the second order peak compared to the first order reflection suggests that inter-platear stacking disorder increased with increasing NEDP content. This could be attributed to the chain length differences of the two molecules, which make disordered multilayers. Even though the X-ray data give

information about structural order normal to the substrate, we were not able obtain any information about the lateral structure (e.g. head) packing. These experiments done at National Synchrotron Light Source in the Langmuir-Blodgett gave some information with how these surfactant molecules were oriented at the substrate interface.

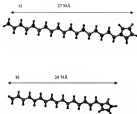


Figure 4-10 The two molecules in their staggered conformation and their calculated lengths. (a) N22DP and (b) N12DP.

Self-consistency of 90% JAGDP with 10% MCDP



Self-consistency of 90% JAGDP and 10% MCDP with 10% MCDP



Self-consistency of 90% JAGDP and 10% MCDP with 10% MCDP



Figure 4-11 Self-consistency of Langmuir-Blodgett of monolayer films: a) 90% JAGDP, b) 90% JAGDP and 10% MCDP, c) 90% JAGDP and 10% MCDP.

Table 4-3 Data obtained from the GED of Langmuir-Blodgett films

Composition	Thickness (Angstrom)	d-spacing (Å)	$d = d_0/2$	SD
100% HEDAP	1.61	48.8	48.8	001
100% HEDAP	1.66	50.8	49.6	002
100% HEDAP	1.78	56.7	56.3	003
100% HEDAP(Average value)			49.6(±0.3)	
80% HEDAP	1.66	47.5	47.5	001
80% HEDAP	1.66	50.8	49.6	002
80% HEDAP	1.80	56.7	56.3	003
80% HEDAP(Average value)			49.6(±0.4)	
60% HEDAP	1.80	48.1	47.1	001
60% HEDAP	1.88	55.4	56.8	002
60% HEDAP	1.93	57.2	56.7	003
60% HEDAP(Average value)			56.4(±0.3)	

4.2.1. Organic Phosphoric Acids Diffraction of the Langmuir Films

X-ray measurements were performed at the Oak Ridge National Laboratory on beamline X-18 of the National Synchrotron Light Source. The experimental setup (Figure 4-4) was described in Section 4.2.3.

At 23°C and at surface pressure 28mN/m, both the HEDAP homopolymer and the copolymer of a 80% mixture of HEDAP and HEDAP showed only one in-phase peak (Figure 4-12). These peaks could be attributed to one-dimensional order along the polymer backbone or one-dimensional order within the polymer chains. The single in-phase peak could also be due to polar head groups arranging in a two-dimensional noninterdigitated hexagonal packing (resulting in one triply degenerate peak). Either model suggests that the long alkyl chains are standing normal to the air/water interface. However, if the sur-

distorted model is used, d -spacings for the 3EDP homopolymer and 50% copolymer calculated as 4.26 and 4.35 Å, respectively (using equations 1-10). If the 2D distorted hexagonal model is used, d -spacings between d -reflections plane for the 3EDP homopolymer and 50% copolymer calculated as 4.26 and 4.35 Å, respectively (equations 1-10). The side length of the hexagon as 4.92 Å for the homopolymer and 5.00 Å for the copolymer (Figure 4-14). The cross molecular area (CMA) that calculated from these values are 30.96 Å² for the homopolymer and 31.45 Å² for the copolymer. From surface pressure-area isotherms, CMA per repeat unit at 21°C and 30mN/m are -19 and -22 Å² for the homopolymer and copolymer (Figure 3-16).

Experiment done with monomer yielded two off-plane peaks for both pure 3EDP ($E_{01} = 1.44 \text{ Å}^{-1}$ and 1.46 Å^{-1} for $E_s = 0.44 \text{ Å}^{-1}$ and 0.56 Å^{-1}) and the 50% mixture ($E_{01} = 1.44 \text{ Å}^{-1}$ and 1.45 Å^{-1} for $E_s = 0.36 \text{ Å}^{-1}$ and 0.20 Å^{-1}) (Figure 4-13). (Since there are off-plane peaks, this suggests that there is a 2D structure with a tilt associated with it. Two cases: a distorted hexagonal model (this could be due to the long alkyl-chain attached between the nearest neighbors) but a definitely eliminates the possibility of tilt toward the nearest neighbors because in-plane peaks were observed (Figure 1-8). Assuming the distorted hexagonal model d -spacing for these data, the following are calculated. The hexagonal bond lengths $a_1 = 4.95$, 4.98 Å and $a_2 = a_3 = 5.02$, 5.05 Å (Figure 4-15) calculation is shown in Appendix A) with a tilt of 17.0°, 11.4° (equations 1-21), respectively, for the 100% 3EDP monomer and the 50% monomer mixture. The CMA that calculated from these values are 30.33 Å² for the pure 3EDP and 31.77 Å² for the 50% mixture. According to the isotherms, corresponding CMA at 21°C and 30mN/m are - 21.1 Å² for the pure 3EDP and -30.8 Å² for the 50% mixture (Figure 3-7).

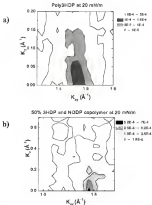
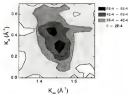


Figure 4-12 Contour plots of the Speckletron X-ray diffraction from the Langmuir monolayers at 25 °C of the polymers. a.) Poly3HDP = 20mM, b.) 50% 3HDP and HGDH copolymer at 20mM.

3HDP monomer at 25 mW/m²

a)

50% monomer mixture of 3HDP and NDOP at 20 mW/m²

b)

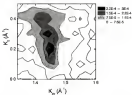


Figure 4-13 Contour plots of the Synchrotron X-ray diffraction from the Langmuir monolayers at 25 °C of the monomers. a.) 3HDP monomer at 25 mW/m². b.) 50% monomer mixture of 3HDP and NDOP at 20 mW/m².



Figure 4-14 The periodicity of the two-dimensional hexagonal model



Figure 4-15 The periodicity of the deformed hexagonal model.

3.3. Conclusion

First, the HEDP is fully formed and calculated the lamellar structure, and the observed lamellar distances were similar, suggesting fully extended (or fully-peeling). The orientation of these surfactant molecules at the air/water interface changes with polymerization. The tail of the monomer molecules directed to water when polymerized. The change in tail end at polymer structure have motivated further investigation of the intermediate structure of these systems. For this reason, a new setup was made, but we were unable to obtain reasonable data. We will continue to explore the use of the MNCSE technique at Argonne National Laboratories. The Langmuir-Blodgett films showed a Y-type deposition. The inter-layer distance and the disorder among layers increased slightly with an increase in the fraction of (HEDP to HEDP).

CHAPTER 3 CONSTRUCTION OF THE INSTRUMENTATION FOR GLAZING INCIDENCE X- RAY DIFFRACTION

3.1 Introduction

The grazing incidence X-ray diffraction (GIXD) data shown in Chapter 4 were done using D₅ P. Dumas setup, and the experiments were performed at beamline X 16A¹⁰⁰ of the National Synchrotron Light Source at the Brookhaven National Laboratories. After construction of the MBXCT¹⁰¹ beamline at the Argonne National Laboratories, a University of Florida team planned to build a new GIXD setup. The setup was commissioned between June 1993 and March 1994 and has been used to obtain some primary data. The instrumentation part of this chapter describes how each component was developed up to the final setup.

3.2 Instrumentation

The whole beamline optical path, including the upstream optics, is a large and very complex system (Figure 3-1,2). Most of the work involving this description was done downstream of the harmonic separator mirror of the beamline. The radiator at the base of the beamline was tunable, and the energy of the X-ray beam could be varied from 4.8 to 10keV.

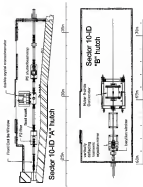


Figure 3-1 Schematic of 10-ID CAT [10-ID] hutch

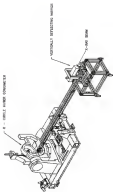


Figure 8-2. Schematic of film symmetrical heads (SSCH) as used in T-Transducer.

After the modulator was tuned for a specific energy, the whole station was misaligned (Fig. 1.11) and reflected to a second Si crystal to guide the beam to the experimental bench, which was 70m downstream. The beam, which missed the experimental bench, contained third and higher harmonics of the fundamental reflection. In order to filter these unwanted wavelengths, a metal-coated flat glass, harmonic rejection mirror, was used. According to the energy used in the experiment, x/11 or an X/8 ring was used. The energy for our experiment was set to 8.05keV, and the 11th ring of the mirror was used to absorb the higher harmonics. The tilted angle of this beam was approximately 1.4mm downwards, but our experiment required an incident angle of 1.4mm to the water/air interface (below the critical angle, 1.44mm for 8.05keV, for total external reflection of the X-rays). A vertical deflecting mirror was used to adjust incident angle to the surface, positioned within a large 8-inch in Hoke™ goniometer, which hold the detector. For simplicity, the mirror will have further discuss three important components: the vertical deflecting mirror, Langmuir trough, and X-ray detector.

1.1.1. Vertical Deflecting Mirror

Three different mirrors were used during commissioning. In our first run with the new setup, there were two options—one was an old harmonic rejection mirror and the other was a flat piece of float glass. The intensity of the flat mirror was good, but the uniformity of the beam was poor (Figures 1-8). This was due to some damage to the metal coating. The piece float glass had a very nice beam profile but gave poor intensity of the

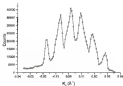


Figure 3-3 Energy profile in the K_x direction, at $E_y = 0$ with poor beam optics

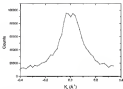


Figure 3-4 Energy profile in the K_x direction, at $E_y = 0$ with improved beam optics

reflected beam. For the next run a platinum strip was coated to the glass, which was used in the run before. The beam profile became narrower and the photon flux of the reflected beam increased (Figure 3-4). The two peaks in the Figure 3-4 correspond to reflected sub-orders of the grating incident beam (section 4.2.3.2).

3.2.3 The Langmuir Trough

The Langmuir trough was designed as it is the center of the 3-axis goniometer (Figure 3-5). Different trough shapes and compression methods were discussed, but finally a rectangular trough with symmetric compression was chosen (Figure 3-6,7). The final trough setup was specified as a part of the dissertation and custom built by KSW Instruments™, Finland (Figure 3-6).

There were two shapes of troughs considered for this experiment. One was a trough with very small footprint ($\sim 10\text{mm}^2$) accessible to the incoming X-ray beam on the liquid surface. In order to achieve this, a small part of the trough needed to protrude so that the X-rays would be continuously incident onto the sample (Figure 3-6a). The small footprint causes less random scattering than a supercell size of the deflected beam. One drawback was that the intensity of the deflected beam would be very small due to the small amount of sample exposure. Since our original Langmuir monolayers were prepared by dissolving materials, we chose to go with a rectangular trough. This system provided a medium footprint ($10\text{--}50\text{mm}^2$) compared to Dr. P. Dutta's setup ($\sim 10\text{--}15\text{mm}^2$) and thus a moderate intensity diffracted beam (Figure 3-6b). In our setup, the width (13mm) of the entrance window of the $K_{\alpha 1}$ filter also limit the amount of diffracted beam observed by the Scintillation detector (Figure 3-6c).

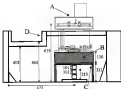


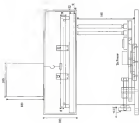
Figure 1.5. The rough setup at the MRCAT terminal. Schematic (top) (for read), A, rough; B, vibrational isolation table (PACON); C, detector bench; D, Fisher-Lewis in perspective; Image (bottom)



Figure 3.6 The automatic harrow covers of the Langston trough



Figure 3.7 The rectangular trough inside the enclosure



1

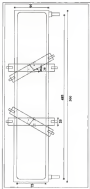


Figure 11 (continued)

Other considerations were focused on during the designing the trough. One was the ability to remove the trough easily. By taking off the top lid of the trough, one could clean the trough in between runs. If the trough needed a thorough cleaning, it could be removed, and a second trough with some dimensions could be inserted without difficulty (Figure 3-18). Cleaning between runs consumes much more time in other setups.^{145,146}

For instance, for overnight cleaning, spending a week maintaining, and redesigning as Dr. P. Datta's trough would be 30000 while the new system would take only 10-15000. The option of a second trough is an advantage of the new system. This feature also could serve for the multi-user environment of the MRCAT beamline; each user could obtain a trough, gas of interest and a Wilkaflex plate which will give them a complete experimental setup without any chemical contamination from other groups.

The regular barrier movement in this setup accommodated approximately 3675mm^2 to 9600mm^2 , a 4:1 compression ratio. Adjustable barriers are another added feature. If one had to compress the barriers close to the center of the trough, they could be adjusted 5-10° in 2° increments. This allows bringing the barriers much closer without blocking the deflected beam. With the barriers at 30°, the area of the monodisper could be changed from 33150mm^2 to 50100mm^2 , a 4.2:1 compression ratio. Compared to P. Datta's setup: 1:1 ratio, that is an improvement.

The temperature of the subphase was kept constant (18.3°C) by recirculating coolant underneath the trough and was measured with a thermocouple inserted into the subphase outside the barriers. The temperature range of the coolant is 3-40°C.

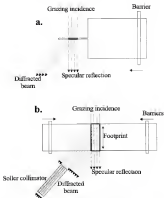


Figure 5-9 Two different shapes of trough: a) Small footprint with single barrier b) Large footprint with two barriers (optimal competition)



Figure 5-10. The second trough that would replace the first for cleaning purposes.

The surrounding windows were built away from the trough to avoid contamination during low temperature runs. The enclosure was airtight, thus, helium gas could be purged to maintain stability and film damage via oxidation.

The complete system could move perpendicular to the incident beam, both horizontal and vertical. The vertical adjustment was important to compensate for the change in the water level. The horizontal adjustment was an added feature to sample the same monolayer but at a different area of the monolayer. The vertical adjustment is very important since it is frequently used during the experiment to compensate for the expansion of the water from the subphase. The motor has very small step resolution ($\sim 1\mu\text{m}$) that the adjustment can be software controlled steps using the KSV software.

All of the five complete trough setups at Datta's Research Lab at University of Florida are purchased from KSV instruments, Finland. All motor drive mechanisms of these troughs are above the water/air interface. But for the special trough that KSV instruments build for the OED setup was design to have the motor drivers on the below the level of water (Figure 5-4) to avoid interference to the monolayer beams. Also this setup

would interfere with Langmuir experiments such as surface potential. The sophisticated control software also allows complex Langmuir experiments.

Another advantage of this system is that the entire trough system can be rotated on a vertical axis when the setup is sitting on the rotatable axis for the 8-chamber Stokes goniometer. This feature gives us ability of rotating the Langmuir film to make sure there is no preferred alignment in the monolayer. Also, steps of χ_{eq} of the films at the V is from 0.2 mN m^{-2} .

The floor vibration which was transferred to the water surface (capillary waves) was minimized using a vibration isolation system (MDC4) purchased from Halcyonics.¹²⁰ Germany. The damping mechanism of MDC4 system has a frequency range of 0.5–100 G/Hz active damping and >100 Hz passive damping. The horizontal and vertical vibrations are acted by 4 piezo-electric actuators. MDC4 was tested using a reflected laser beam, which was projected to a wall ~125 away from a water surface and the error was reduced dramatically.

Table 4-1 Summary of information of several different CDD setups

Researcher	Synchronous source	Wavelength (Å)	Photopair (nanosecond)	R_{eq} - $4R_{\text{eq}}$ reflection	R_{eq} resolution (mrad)	Detector
SW1 ¹²¹	DMR25, Hamburg	1.27	1ns20	Solar film	1.50	PSD
AL20 ¹²²	NELLS, New York	1.45		Solar film	1.0	PSD
DL1 ¹²³	DLRL, Orsay	1.48		Solar film	0.4	PSD
DL1B ¹²⁴	DLRL, Orsay	1.484		Solar film	1.40	PSD
AL4A ¹²⁵	NELLS, New York	1.54	10x150	Solar film	2.5	Phot.
DL2 ¹²⁶	DLRL, Grenoble	1.5715		Analyzer	0.54	Phot.
MAGAT	APS, Chicago	1.54	10x75	Solar film	1.68	Phot.

3.2.3 X-ray Detection

As seen in Section 4.3.3, there was a vast difference in the diffraction of the monomers of monomers and the polymers. Our goal was to build a system enabling us to detect the change in real time during the polymerization reactions and find the intermediate crystalline structure of these materials. Since earlier results were obtained via a point detector, we investigated the possibility of having linear detectors to measure the diffraction. The construction of the detectors and the results are discussed below. Our goal was to use both (MEL-1/FB-90 (Linear PSD with 3mm diameter window) and (DPS-1/CB-100 (Curved PSD with 3mm wide and 120 mm-dia window with a radius of 200mm). The main advantage of this system was the ability to rapidly do a rough scan with the curved detector and then a high resolution scan with the LPS 90 such that a range of K_{α} data could be obtained for a given $K_{\alpha 0}$. Both detectors could be mounted on the detector arm on the Fisher 4-cryto goniometer. The first suggestion was to mount both detectors as shown in 4 (Connecting arm is in a vertical plane) as Figure 3-11, but the offset of the detectors was about 30°, which was too large to accommodate in such a limited space. The second option was to mount the detectors side by side (Figure 3-11B). An appropriate mount from the travel to the detectors was machined, and a slit (with angular acceptance of 3.54°) for the curved detector was built to improve S/N. An improvement was not using a Langmuir-Blodgett film.

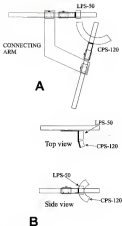


Figure 3-11. Schematic of positions of linear detectors

Since we did not have the budget setup at this time, we used 30 multilayers of LiF film of Shonka used in the reflection mode. The goal was to maximize the response of these detectors at a reasonable cost. If the sensitivity of both point and the line detectors were the same, response time would be reduced drastically. For example, if the CTS-120 detector is 300mm away from the sample, then acquisition of a range of $0.1\text{--}10^{-1} \text{ K}_\alpha$ for each step of K_α . But angular acceptance of the diffracted beam (both in K_α and K_β direction) had to be considered. Compared to point detector holder slots (parallel plates), the linear detector holder slots (radial plates with an appropriate focal length) are much more complex and had to custom built.

On the other hand, a point detector integrates scattering over a large area of the multilayer. Reducing the beam width (beam windows of the line detectors), greatly decreases the scattering cross section. Furthermore, any gain in detector speed corresponds to a reduction in the amount of time a given multilayer is exposed to radiation per experiment. The intensity of the monochromatic X-ray beam at the MRCAT experimental bench is about 5×10^{20} photons/sec, significantly higher than that of NLS (1×10^{20} photons/sec) and many orders of magnitude higher than any laboratory source (Co K_α) at 10^9 .

All of the hardware (two detectors, XRD box, modules, Computer, Interface card, and cables) for the detector function was taken to Argonne National Laboratories. A 5 liter cylinder of detector gas (10% Nitrogen and 90% Argon) was purchased from Advanced Gas Company. In order to achieve the same number of counts as the point detectors, the linear detectors took 30 times longer. In fact, the detectors performed very

poorly. This class of laser detection was temporary palatable, and the experiment was then focused on a quasi-director system.

Two magnification detectors were purchased from Calsonics and used as the point detectors. Horizontal and vertical 30-linr slits were mounted on the front of the detectors, which measures the diffraction. The angular acceptance of horizontal slit (plane K_{\perp}) was 2.34° (0.0448 λ^{-1}) and of vertical slit (plane K_{\parallel}) was 0.089° (0.0016 λ^{-1}). The detector and the two 30-linr slits were attached to one a-rail with a mount bolt at the machine shop. Another detector was supposed to measure the reflected beam and was placed behind the 8-coude prismometer. A special table was built at the machine shop in the chemistry department and taken to the MIT/CAT beamline (figure 5-12). The results obtained from this setup are discussed below and compared with the Chao group's setup, which was discussed in Section 5.3.3.



Figure 5-12 Special spread table built for the CID setup

3.3 Results and Discussion

The alignment of the setup was exactly the same as the Dotto group's setup as described in Section 4.3.3 except for some additions to the rough design and a different beamline. The optical path (source and slits) of the X-ray beam is identical to Figure 4-6. The diffraction pattern of C20 acid ($\text{C}_{20}\text{H}_{39}\text{O}_6$) at $T = 2^\circ\text{C}$ and $2\theta = 30\text{mN}$ was used as a standard and is shown in Figures 3-12. Both sets of data were obtained at $K_\alpha = 0$. Also Figure 3-14 shows a main scan of C20 acid where both peaks of the standard are in view. These peak values ($K_\alpha = 1.568\text{\AA}^{-1}$ and 1.618\AA^{-1}) agreed with the literature values, so our setup was fully contaminated. The signal-to-noise (S/N) of the graphs in Figure 3-13 are 41 (top) and 145 (bottom). And the signal-to-background (S/B) for the same graphs are 3.3 and 12.9. The difference in FWHM of these two graphs is due to difference of the temperature. If we design the standard procedure to obtained peaks at 2°C , what would we get 2°C since the peak position still remains the same.²⁶ But according to published data,²⁶ FWHM of the peak at $K_\alpha = 1.503\text{\AA}^{-1}$ was 0.021\AA^{-1} at $T = 6^\circ\text{C}$ compare to our value of $0.016 \pm 0.003\text{\AA}^{-1}$ at 2°C (Figure 3-12).

The next step was to reproduce the results of JEDF, which were discussed in Chapter 4. Using the same Langmuir trough and detectors were used at NSLS (Dotto's setup) but performing the experiments at MRCAT beamline produced a different diffraction pattern than before (Figure 3-15). The peaks which were off-plane have now moved to α -plane ($K_\alpha = 0$). Similar results were seen when the experiments were done at MRCAT using the new setup. Figure 3-16 shows the diffraction of JEDF at $K_\alpha = 0$ that was obtained from the new setup. These results are very similar to the data we obtained

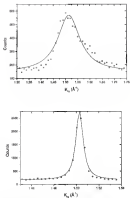


Figure 3-12 Diffraction pattern of the standard (JDE std) 304H16. The line is the Lorentzian fit. Top: Data collected [at 19°C] from Delta's setup. Bottom: Data collected [at 19°C] from our own setup.

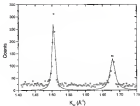


Figure 4-14. Diffraction pattern of the standard P2VP sample: 5% and 10% films. The fact is the Correlation 15.

for the polymerized product of NVEs (Figure 4-12). Since the bond intensity of APS is much higher than NVEs, the competing reactions could react with hydroxyl and hydrogen radicals, which are being produced when X-rays are irradiated on water. The reaction would produce similar to products. Oxidation state measurements of aqueous systems were done using ELAP5 at MRCAT beamline and many broad redox potentials were found.^[40] Further information on effects of radiation on water can be found in the following books: *An Introduction to Radiation Chemistry*^[41] and *The Radiation*

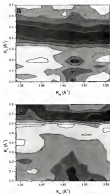


Figure 3-23 Correlation plots of the Synchrotron X-ray diffraction from the Langmuir monolayers at 25 °C of the monolayer (Data was obtained with the Data's setup and at PGM-CAT beamline). (a.) 20°C monolayer at 20mN/m, 75-100% monolayer mixture of 30DAP and H0DAP at 10mN/m.

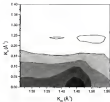


Figure S-14 Contour plot of the 2D synchrotron X-ray diffraction from the Langmuir monolayers at 25 °C of the 80% H₂O/20% D₂O (Data was obtained with the new setup and at MRC will be coming).

Chemistry of Water ¹²⁸ One way to confirm this result would be it to alternate the primary beam and run the same experiment. Another way is to combine some bulk sensors with X-rays and analyze the product. Having better insight enclosures with a good Water purge could reduce the amount of oxygen in molecules in the enclosure that will reduce the oxidation process.

Due to time constraints, my experimental work on the H2O/D2O system was stopped at this point. A number of aspects of the experiment could be modified to improve the data quality however:

The first suggestion to improve the current setup is to inspect the trough vacuum thoroughly to assess the air-tightness of it. Having a separate cylinder of helium for trough setup would help to control the flow and pressure of helium inside the vacuum. The helium lost should be filled to high water, so a stream of water saturated helium could be sent to the vacuum. This procedure would help reduce the evaporation of water from the subphase.

The vibration isolation system is below the Langmuir setup. The vibration caused by the coolant flow underneath the trough cannot be damped by the MGD4 system. But having a dissymmetric element such as Pultrac cooler could eliminate the vibration. Even though cooler elements were very small in size, currently a square (50x50mm) with thickness 3mm's Pultrac element with efficiency of 1 kW could be purchased.¹⁸⁰

As shown in the Figure 1-56, the width (11mm) of the Soller slit is limiting the amount of scattering from surface, which is observed. The amount of signal can be increased by having Soller slit collimator with the same resolution but with wider (roughly the width of the trough entrance window). But the detector window is a circle with a diameter of 40mm. In order to collect all the photons, which were collimated with K_{α} and K_{β} Soller slit, a focusing optic¹⁸¹ should be used. Current Soller slit were purchased from Oskay Industries. The best resolution Soller slit were used in the Kay detector. Custom build ones were considered, but they were very expensive.

Since this trough setup was used only three times to date, it is still on the development stage. But the resolution of the measured peak confirms that this setup has a very good resolution. The modifications discussed in this section could be applied and even better performance could be achieved by this system.

5.4. Conclusions

The new grazing incidence X-ray diffraction setup was a fully operational instrument. It produced very good results on CDS and compared to the Delta group's setup. The results obtained on the WEP at the MSCAT beamline were different from the results obtained at NSLS. This could be due to the polycrystalline product, which was created by oxidation of the monomer.

As described in the earlier sections, the setup consists of several different devices applicable to its flexibility.

APPENDIX A
CALCULATION OF HORIZONTAL BOND LENGTHS OF A DEFORMED
HEXAGONAL LATTICE



Fig. 1. Deformed hexagonal lattice

$$a_1^2 + a_2^2 = a_3^2$$

Where a_1 , a_2 , and a_3 are horizontal bond lengths of the lattice structure. Parameter α_1 and α_2 obtained from the X-ray data using the equations 1-10. According to the above drawing:

$$\sin \alpha = \frac{d_1}{a_1} \quad \cos \alpha = \frac{d_2}{a_1} \quad (A-1)$$

$$\frac{d_1}{a_1} = \frac{d_2}{a_1} \quad (A-2)$$

Solving for a_1

$$a_1 = \frac{d_1 d_2}{d_1} \quad (A-3)$$

But by the Pythagorean theorem:

$$a_1^2 = d_1^2 + \left(\frac{d_2}{1}\right)^2 \quad (A-4)$$

By substituting value of a_1 from equation A-3 in the A-4 equation,

$$a_1^2 = d_1^2 + \left(\frac{d_1 d_2}{d_1}\right)^2 \quad (A-5)$$

By simplifying:

$$a_1^2 = \frac{d_1^2 d_2^2}{(d_1 d_2^2 - d_1^2)} \quad (A-6)$$

Since d_1 and d_2 are known, a_1 can be calculated. Then a_2 can be easily obtain by substitution in equation A-3

APPENDIX B **EXPERIMENT SETUP-CHECKLIST FOR ALIGNMENT PROCEDURES FOR** **GRATING INCIDENCE DIFFRACTION OF LANGMUIR MONOLAYERS AT THE** **MARCATI BEAMLINE**

Step 1. _____ Equipment Setup

- Connect all the cables, check all the cables.
- Connect all rough controls, calibrate the balance, run a quick software-of-mouse test
- Connect the temperature buffer and check the temperature control
- Move balance path after the 1st mirror to the rough where are my optics
- Check the room. Also try to have 2 tanks one to the 1st mirror and other to the lens and the rough.

Step 2. _____ Incident Angle Alignment in L.A. area

- Set the energy to $Cu K\alpha_1$, 1000 eV
- Mirror 1 (M1) energy scan to find the energy cutoff
- Scan M1 again at incident angle θ_i find to find the cut-off energy for 1st harmonic. (Keep 1 & 2 files doing)
- Find and go to the maximum angle with 1st harmonic rejected.
- Adjust the M1 height to get the maximum intensity
- Run paper at the center of the Baker (CH), incident beam separates "top-top"
Measure the distance from the downstream edge of the M1 to CH. Calculate the angle (θ_{CH}) respect to Primary Beams, which is pretty much horizontal.
- Six scan (what should be the size of the first slit, 1000 measured) to block the primary beam and to define the 1st reflected beam
- Adjust mirror 2 (M2) so that it is roughly horizontal.
- Do a height scan of the M2, and go to the position with M2 cut-off the beam.
- M2 tilt scan to find the direction parallel to the 1st reflected beam. Beam should look like a peak, but not a plate. Go to that tilt.
- M2 height scan to get intensity half of the maximum intensity. Go to that height.

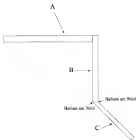
- Now we have to get $(\theta_{\text{ref}} - 2)$ read angle deflected upwards to get 2 read on the water surface. So increase tilt of M2 to get the desired line separation on the fluorescent paper.
- Turn paper at the center of the Fluor (CH), measure line separation "two inside marks". Measure the distance from the downstream edge of the M2 to CH.
- At this moment, the angle between M2 and the 1st reflected beam is $\theta_{\text{ref}} = (\theta_{\text{ref}} - 2) + 2$.
- Adjust the height and the horizontal center of the Fluor to the 2nd reflected beam.
- Minimize the reflection from the mirror by adjusting the height.
- Make sure that Windows isolation table is on.
- Bring the water surface to the beam.
- Observe two lines (bring the trough to block the beam, then tilt the M2 to get the beam back, lower the trough again to block the beam, then tilt the M2 again. Repeat until you get a reflection).
- Adjust the sample to get equal intensity.
- Turn paper and measure the line separation "two inside marks".
- Check the angle.
- Adjust the M2 tilt, check the angle.
- De-water scan and block the 2nd reflected beam (this scan 1000 scans).
- Narrow the 2nd slit to define the reflected beam from M2.
- Narrow the 2nd slit to define the reflected beam from sample.
- Finish all the mirror positions.

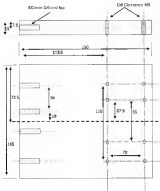
Step 3. _____ (2nd Alignment with B₁ and K₁ Alignment)

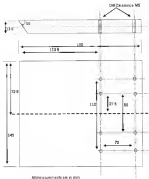
- Move 20 (low) into the first beam (alignment only) scan the horizontal beam profile.
- Scan the maximum at $K_{\text{ref}} = 0$.
- Scan the vertical beam profile and set max at $K_{\text{ref}} = 0$.
- Move 20 to about 2\AA^{-1} .
- Place B₁ powder sample at the beam so that 20 can see it.
- Scan without K₂ filter slit for 111 peak (should be at 2.005\AA^{-1} , scan for 110 peak (2.275\AA^{-1})).
- Set motor values of low in the correct positions.
- Scan B₁ again as usual.
- Scan + standard B₁ (K_{ref} scan), check the positions.
- Insert the K₂ filter slit.
- Perform a K₂ scan, and set the maximum of the peak at $K_{\text{ref}} = 0.02$.

Note: K_{ref} used at 2°C at H₂O/D₂O peaks are at $K_{\text{ref}} = 1.58\text{\AA}^{-1}$ and 1.68\AA^{-1} (both at $K_{\text{ref}} = 0$)

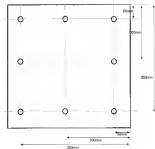
APPENDIX C
MECHANICAL DRAWINGS OF DIFFERENT COMPONENTS WHICH WERE USED
IN THE 3D EXPERIMENT







All Holes are M6 Thread.



REFERENCES

1. McDonald, A.G. / *System A-2: Seven-Dimensional Systems and Molecular Electronics*; Morgan, R.M., et al., Eds.; Plenum Press: New York, p. 353, 1993.
2. Ananyevskii, S., Challen, G.K., Gerasimova, G.A., Fletcher, D. / *Electronsf. Chem.* **1994**, *177*, 245.
3. Clark, K., Ferry, M., Truong, V.T. / *Synth. Met.* **1998**, *94*, 213.
4. Bille, J., Hagmann, J.A., Wagner, G. / *Molecular Chem. Superconduct.* **1989**, *18*, 705.
5. Wu, M., Zhu, C., Yang, J., Shi, C. / *Synth. Met.* **1999**, *98*, 157.
6. Sanders, B.B., Fleming, B.J., Murray, K.S. / *Chem. Mater.* **1995**, *7*, 1482.
7. Zhou, H.C., Davis, R.S. / *This Solid/Thin* **1992**, *219*(11), 395.
8. Yama, A., Kuroki, T., Ogasaw, F. / *Macromolecules* **1989**, *22*, 424.
9. Price, T.J., Windsor, M.J., McCullough, R.D. / *Macromolecules* **1994**, *27*, 1654.
10. Kong, K., Sauer, B.B., Salazar, M.F. / *Chem. Mater.* **1996**, *8*, 33.
11. Bolman, A.G.M., Samwel, L., Meekes, D., Clough, S., Tripathy, S., Inagaki, T., Yang, X.Q., Stokholm, T.A., Okamoto, Y. / *Synth. Met.* **1995**, *68*, C157.
12. Sigmond, W.M., Bailey, T.B., Hays, M., Sanders, B., Kroll, W., Davis, R.S. / *Langmuir* **1995**, *11*, 3155.
13. Zhou, H., Chen, K., Smith, C., Davis, R.S. / *Molecular Chem. Superconduct.* **1992**, *21*, 625.
14. Bolman, A.G. / *Davis, R.S. Polym. Prepr. (Am. Chem. Soc. Div. Polym. Chem.)* **1994**, *35*(2), 345.

6. Marlow, C.A., Fendley, M.P., Lacey, M., Rogers, G. *The Solid Film* 1996, 284, 179
7. Fench, M.T., Rieflinger, A., Finner, B., Rogers, G., Coudane, P. *The Solid Film* 1999, 284, 234
8. Sargent, W.M., Wessenden, G., Mearns, C., Byers, S., Ebra, H., Eshen, M.Z., Kuhn, J., Wagner, G., Dunn, R.S. *Langmuir* 1999, 15, 4023
9. Franklin, B. *Philos. Trans. R. Soc. London* 1778, 68, 442
10. Rayleigh, L. *Proc. R. Soc. London* 1890, 47, 364
11. Rayleigh, L. *Nature* 1891, 43, 477
12. Langmuir, I. *J. Am. Chem. Soc.* 1916, 38, 2221
13. Langmuir, I. *J. Am. Chem. Soc.* 1917, 39, 1848
14. Langmuir, I. *Trans. Faraday Soc.* 1919, 15, 62
15. Hodge, K. *J. Am. Chem. Soc.* 1917, 39, 161
16. Hodge, K. *Phys. Rev.* 1922, 19, 568
17. Ebdell, E. *An Introduction to Surface Chemistry*, The University Press, Cambridge, 1939
18. Adams, H.E. *The Physical Chemistry of Surfaces*, 1st ed., Oxford University Press, Oxford, 1940
19. Harkins, W.D. *The Physical Chemistry of Surface Films*, Reinhold, New York, 1952
20. Adamson, A.W. *Physical Chemistry of Surfaces*, 4th ed., John Wiley & Sons, New York, 1962
21. Gosses, G.L. *Reinhold Monolayer on the Liquid-Gas Interface*, John Wiley & Sons, New York, 1968
22. Ulman, A. *An Introduction to Ultrathin Organic Films*. From Langmuir-Blodgett to Self-assembly, Academic Press, Boston, 1991

- ¹¹ Kubota, G. *Langmuir-Blodgett Films*, Plenum Press, New York, 1980.
- ¹² Jeng, M. *Langmuir-Blodgett Films: An Introduction*, Cambridge University Press, New York, 1988.
- ¹³ Kuhn, H. *Proc Appl. Chem* 1963, 11, 345.
- ¹⁴ Kato, J.R., Szwarc, P.J. *Macromolecules* 1978, 11, 593.
- ¹⁵ Ott, G. *Proc. R. Soc. London, Ser. A* 1933, 153, 129.
- ¹⁶ Wilks, L. *Am. Phys.* 1963, 119, 177.
- ¹⁷ Heng, D., Milnes, D. *Thin Solid Films* 1981, 79, 64.
- ¹⁸ Twest, A.G., Gault, G.L., Bellamy, W.D. *J. Chem. Phys.* 1944, 12, 279.
- ¹⁹ Gethiger, H., Milnes, D., Mayer, H. *J. Chem. Phys.* 1963, 79, 770.
- ²⁰ Lee, G., Wagon, G., Taka, B. *Thin Solid Films* 1986, 13, 77.
- ²¹ Twest, A.G. *Rev. Sci. Instrum.* 1946, 17, 1412.
- ²² Langmuir, I., Schaefer, V.J. *J. Am. Chem. Soc.* 1949, 71, 1871.
- ²³ Datta, M.K., Malik, A., Balcer, A.G., Wang, K.G., Datta, P. *Langmuir* 1997, 13, 6347.
- ²⁴ Treloar, R.H., Wiles, C.B. *J. Phys. C* 1968, 15, L15.
- ²⁵ Yano, A., Kawakita, Y., Ohta, A., Tanaka, M. *Langmuir* 1997, 13, 409.
- ²⁶ Kawamura, S., Tanaka, T., Sato, S., Inoue, Y., Kato, K. *J. Am. Chem. Soc.* 1993, 115, 600.
- ²⁷ Bradley, D., Venzl, R.H., Ludenberger, H., Roth, S. *Polymer* 1988, 29, 1709.
- ²⁸ Nagata, D., Landa, R.D., Kinsinger, H. *Macromolecules* 1977, 10, 1119.
- ²⁹ Tanaka, M., Yamashita, H., Sugiyama, T. *Jpn. J. Appl. Phys.* 1988, 27, L258.

- ¹⁴ Mulliken, R. *Chemistry at Iorophore*, Academic Press, New York, 1991.
- ¹⁵ Stevens, H. *Zeitschneue Anal. Chem.* 1913, 261.
- ¹⁶ Ter-Monastier-Savign, L., Frigolant, J. *Ann. Rev. Chem. Ed. (Paris)* 1953, 33, 109.
- ¹⁷ Baron, E.W., Thomas, W.N., Fieser, H.B., Rice, S.A.; Lee, B., Peng, J.B.; Krimm, J.B., Dora, P. *J. Chem. Phys.* 1990, 93, 3357.
- ¹⁸ Goodrich, P.C. *Proc. Int. Congr. Inf. Sci.*, 7th 1997, 1, 13.
- ¹⁹ Barth, G.; Rogers, R.B.; Jackson, C. *Anal. Chem.* 1994, 66, 4458.
- ²⁰ Bykowski, C.; Bush, M.D. *Anal. Chem.* 1996, 68, 1618.
- ²¹ Allcock, H.R., Lewis, F.W. *Contemporary Polymer Chemistry*, 2nd ed., Plenum Hall, Englewood Cliffs, NJ, 1980.
- ²² Wilczek-Vera, G.; Davis, P.D.; Bamberg, A. *Macromolecules* 1994, 27, 6026.
- ²³ Johnson, D-C.; Li, L. *Anal. Chem.* 1997, 69, 6197.
- ²⁴ Selinger, A.; Neugebauer, D.; Scherling, J. *Rapid Commun. Mass Spectrom.* 1999, 13, 2419.
- ²⁵ Kern, M.; Höltschamp, F. *Anal. Chem.* 1999, 71, 1299.
- ²⁶ Tanaka, K.; Waki, H.; Ito, Y.; Arita, S.; Yoshida, Y.; Yoshida, T. *Rapid Commun. Mass Spectrom.* 1998, 12, 131.
- ²⁷ Johnson, D-C.; Li, L. *Anal. Chem.* 1998, 70, 2711.
- ²⁸ Brown, R.S.; Lewis, J.J. *Anal. Chem.* 1999, 71, 1799.
- ²⁹ Myers, J.A.; Dancow, R.J.; Miles, R.E. *Rapid Commun. Mass Spectrom.* 1997, 11, 49.
- ³⁰ Wilczek-Vera, G.; Yu, Y.; Waddell, R.; Davis, P.D.; Bamberg, A. *Macromolecules* 1999, 32, 2180.
- ³¹ Naficy, M.W.F. *Mass Spectrom. Rev.* 1999, 18, 309.

- ⁶⁰ Hillenkamp, F.; Karas, M.; Becks, R.G.; Chaz, B.T. *Anal. Chem.* 1978, 50, 1190A.
- ⁶¹ Takacs, F.L.; Person, M.D.; Wiland, R.M.; Wells, F.C.; Balagurusamy, A.L.; Bahrwald, H.A. *Rapid Commun. Mass Spectrom.* 1989, 13, 1170.
- ⁶² Barlow, R.D.; Watson, C.H.; Eyles, J.R.; Lang, G.L.; Powell, D.R.; Avery, M.Y. *Rapid Commun. Mass Spectrom.* 1987, 11, 643.
- ⁶³ Bendler, K.; Kuchemann, R.; Dreier, R. *J. Am. Soc. Mass Spectrom.* 1990, 10, 1111.
- ⁶⁴ Carter, R.J. *Time-of-Flight Mass Spectrometry: Instrumentation and Applications in Biological Research*, American Chemical Society, Washington, DC, 1997.
- ⁶⁵ Hagerfeldt, M.C.; Fox, G.B.; Smith, L. *Anal. Chem.* 1993, 65, 3304.
- ⁶⁶ Dolu, M.; Mark, L.L.; Hesse, R.L.; Nohley, R.C.; Ferguson, L.D.; Allen, M.D. *J. Chem. Phys.* 1988, 88, 3268.
- ⁶⁷ Yanagida, M.; Fox, J.B. *J. Phys. Chem.* 1988, 92, 4451.
- ⁶⁸ Wang, J.F.; Meng, C.K.; Fox, J.B. *J. Phys. Chem.* 1989, 93, 546.
- ⁶⁹ Nakas, T.; Fox, J.B. *J. Am. Chem. Soc.* 1992, 114, 3241.
- ⁷⁰ Yu, C. *Handbook of Eco-Evolutionary Chromatography: Chromatography for System Series*, Vol. 45, Marcel Dekker Inc., New York, 1995.
- ⁷¹ Horning, E.G.; Horning, M.G.; Carroll, D.L.; Dreier, L.; Siffertell, R.H. *Anal. Chem.* 1979, 51, 936.
- ⁷² Horning, E.G.; Carroll, D.L.; Dreier, L.; Hagerfeldt, K.D.; Horning, M.G.; Siffertell, R.H. *Advances in Mass Spectrometry in Biochemistry and Medicine*, Ferguson, A., et al., Eds., Spectrum Publications, New York, Vol. 1, p. 1, 1978.
- ⁷³ Norrén, W. In A. Applications of LC/MS in Environmental Chemistry, Barcelo, D., Ed.; Elsevier: Amsterdam, Vol. 25, p. 3, 1996.

81. Morris, C.H., Smith, J.W., Bryant, D.W., McCarty, B.B. *J. Chromatogr. A* **1999**, *855*, 13.
82. Kuster, L., Fekken, R., Yin, P. *Rapid Commun. Mass Spectrom.* **1999**, *13*, 2439.
83. Altan, I. *J. Mass Spectrom.* **1999**, *34*, 127.
84. Chaudras, B.A., Kuster, K.D., Kucharski, R.L., Stevens, J.M. *J. Am. Chem. Soc.* **1999**, *121*, 11135.
85. Voths, D., Mauch, P., Kucharski, R. *Rapid Commun. Mass Spectrom.* **1999**, *13*, 2511.
86. Kucharski, R., Fekken, T., Kucharski, R., Liu, K., Rostek, R. *Rapid Commun. Mass Spectrom.* **1999**, *13*, 1399.
87. Kucharski, R., Wang, K., Liu, B.C. *Eur. Mass Spectrom.* **1999**, *4*, 625.
88. Jepp, M.J., Jennings, K.R., Jurek, C.B., Haddleton, D.M., Jackson, A.T., Tait, R.T., Stevens, J.H. *Rapid Commun. Mass Spectrom.* **1997**, *11*, 37.
89. Kucharski, R., Lehman, R., Kuster, K. *Eur. Mass Spectrom.* **1998**, *3*, 421.
90. Sadtley, K.G., Fekken, R.H., Haddleton, D.M. *Macromolecules* **1996**, *29*, 8042.
91. Goh, M.C., Fung, A.B., Auman, R.C., Fung, Y., Zhao, M.Y., KEE, D.H. *Macromolecules* **1996**, *29*, 7354.
92. Wilczek-Vera, O., Yu, Y.S., Waddell, K., Davis, P.O., Rimmberg, A. *Rapid Commun. Mass Spectrom.* **1999**, *13*, 761.
93. Flory, P.J. *Principles of Polymer Chemistry*; Cornell University Press: Ithaca, 1953.
94. Rayfield, J.C. *Polymer Sequence Determination*; Academic Press: New York, 1977.
95. Niles, M.W. *Rapid Commun. Mass Spectrom.* **1996**, *10*, 1612.
96. Jackson, C., Lyons, B.B., McFie, C.H. *Anal. Chem.* **1996**, *68*, 1330.
97. Ragusa, V.M., Stillwell, H., Della, F. *Eur. Med. Chem.* **1999**, *34*, 779.

- [99] Kjær, K., Ahlström, P., Høhn, C.A., Lachkar, L.A., Mikkelsen, E. *Phys. Rev. Lett.* **1987**, *58*, 2228.
- [100] Datta, P., Peng, J.P., Lee, B., Kallman, J.R., Puskas, M., Georgopoulos, P., Ehrlich, S. *Phys. Rev. Lett.* **1987**, *58*, 2229.
- [101] Eisenberger, P., Mann, W.C. *Phys. Rev. Lett.* **1981**, *46*, 1081.
- [102] Ahlström, J., Jørgensen, B., Kjær, K., Lavelle, P., Lohr, M., Leisnerwig, L. *Phys. Rev.* **1994**, *348*, 207.
- [103] Sauer, U.B., Cramer, W.B., Suter, U.W. *Langmuir* **1994**, *10*, 3407.
- [104] Järnqvist, K.E., Samdal, B.J., Pettersen, L.A.A., Ingman, O., Johansen, T., Færevik, R. *Surf. Sci.* **1999**, *431*, 361.
- [105] Furlan, P., Callaway, M., Rombles, F. *Langmuir* **1999**, *15*, 1340.
- [106] Kagan, V.M., Logovoy, O.B. *Phys. Rev. E Phys. Plasma, Fluids Solid, Interfacial Top.* **1999**, *59*, 2217.
- [107] Jones, R., Goodfield, R.H., Bourke, A., Hodges, P. *Thin Solid Films* **1988**, *151*, 115.
- [108] Snow, A., Burger, W.A., Klotz, M., Wolden, H., Jones, N.L. *Langmuir* **1999**, *15*, 571.
- [109] Schuster, U., Snow, K.E., Klotz, H. *J. Chem. Phys.* **1994**, *101*, 3008.
- [110] Enay, F.W., Miller, L.L., Bak, S.P., Fendley, T.H., Christophel, W.C., Kim, J.R., Upham, R.A. *J. Am. Chem. Soc.* **1998**, *120*, 6441.
- [111] Ferry, M.C. *Thin Solid Films* **1952**, 25(77), 417.
- [112] Zhu, D.G., Chu, G.P., Ferry, M.C., Harris, M. *Surf. and Interfaces* **1995**, *11*, 163.
- [113] Martin, A.S., Scudiero, J.B., Ashwell, G.J. *Phys. Rev. Lett.* **1993**, *70*, 111.
- [114] Salas, B. *Adv. Mater. (Weinheim Ger.)* **1990**, *2*, 222.

- [1] Kuhn, H., Illers, D., Maier, H. *Physical Methods of Chemistry*, John Wiley, New York, 1972.
- [2] Kuhn, H. *Thin Solid Films* 1981, 99, 1.
- [3] Sogawa, T., Endow, S., Kuroki, K., Iwamura, H., Yoh, K. *J. Am. Chem. Soc.* 1986, 108, 368.
- [4] Fendia, S.P., Smith, K.A. *Thin Solid Films* 1983, 99, 129.
- [5] Cheng, T.R., Kozak, W.J., Haglund, H.B., Sargent, V.T. *Materials Science of Liquid-Crystalline LCD Symp. Ser.* 1983, 269, 21.
- [6] Blum, L.M., Maltsev, L.V., Salomon, R.G., Yoda, S.G. *Sov. Phys. Solidstate* 1982, 24, 1923.
- [7] Triggall, R.F. *Order in Thin Organic Films*, Cambridge University Press, Cambridge, 1984.
- [8] Hong, K., Palmer, M.F. *Thin Solid Films* 1983, 105, 187.
- [9] Fokker, C., Lenz, G., Wagner, G. *Microanal. Chem. Phys.* 1990, 160, 2627.
- [10] Mizutani, H., Kurihara, S. *Microanal. Chem. Phys.* 1991, 166, 2073.
- [11] Sun, G.H., Soyuz, C.H., Connor, D.M., Colford, D.M. *Langmuir* 1994, 10, 3310.
- [12] Myers, R.B. *J. Electron. Microsc.* 1996, 35, 43.
- [13] Kato, S., Suzuki, Y., Goshima, G.F. *Jpn. J. Phys.* 1988, 24, 217.
- [14] Sato, J. PhD thesis, University of Illinois, 1989.
- [15] Cao, Z., Qi, M., Chen, S. *J. Electroanal. Chem.* 1994, 373, 141.
- [16] Liu, F., Lewis, R.S., McCullough, S.D. *Macromolecules* 1999, 32, 5777.
- [17] Mochales, M.B. *Rapid Commun. Mass Spectrom.* 1998, 12, 639.
- [18] Ichi, G., Tsuchi, S., Morita, M. *J. Polym. Sci. Part A Polym. Chem.* 1995, 33, 1961.

- 104 Weston, S., Ellis, G., Finkelsch, J. *Appl. Comput. Mater. Spectrosc.* **1998**, *12*, 1371.
- 105 Cooper, R., Burdington, A.L. *Appl. Comput. Mater. Spectrosc.* **1998**, *14*, 53.
- 106 Nelson, M.W., Malocha, E. *Appl. Comput. Mater. Spectrosc.* **1995**, *11*, 1184.
- 107 Lee, H., Lee, W., Chang, T., Cho, S., Lee, D., N. H., Namikawa, M., Matsuy, J.W. *Physicochemistry* **1999**, *12*, 4143.
- 108 Materials Research Collaborative Access Team (MRCAT) Home Page <http://mx.scripps.ucla.edu/> (accessed Jan 2000).
- 109 Advanced Photon Source Home Page <http://aps.anl.gov/welcome.html> (accessed Jan 2000).
- 110 Argonne National Laboratory Home Page <http://www.anl.gov/> (accessed Jan 2000).
- 111 Lee, H. *X-ray Diffraction Studies of Polyols and Alcohol monolayers on the Surface of water (Liquid Films)*, Ph.D. Dissertation, Northwestern University, 1999.
- 112 Suk, M. *Synchrotron X-ray Studies of monolayers at aqueous interface and on Solid Surfaces*, Ph.D. Dissertation, Northwestern University, 1991.
- 113 Durkin, M.K. *Synchrotron X-ray diffraction studies of Langmuir monolayers* Ph.D. Dissertation, Northwestern University, 1993.
- 114 X-14A and Synchrotron X-ray Beamline at NSLS, BNL. <http://f1130.bnl.gov> (accessed Jan 2000).
- 115 National Synchrotron Light Source Home Page <http://www.snl.bnl.gov/> (accessed Jan 2000).
- 116 Brookhaven National Laboratory Home Page <http://www.bnl.gov/> (accessed Jan 2000).
- 117 Thomas, R.H., Bacon, S.W., Marsh, P., Rice, S.A. *J. Chem. Phys.* **1997**, *106*, 1034.

- [140] Kohl, T.L., Mayrhofer, J., Brown, P.R., Ryan, K., von Nottow, A., Lee, K.Y.C., Oden, B., Bruckenstein, M., Smith, G.B. *J. Am. Chem. Soc.* **1999**, *121*, 7582
- [141] Mayrhofer, J., Papadimitrakis, K., Brown, W.G., Ryan, K., Ah-Medien, J., Lohr, M., Lammert, L. *Chem.-Ber.* **1999**, *1*, 704
- [142] Home page of Heliogenix: <http://www.heliogenix.de/> (accessed Jan 2000)
- [143] Mayrhofer, J., Papadimitrakis, K., Brown, W.G., Ryan, K., Ah-Medien, J., Lohr, M., Lammert, L. *Chem. Ber.* **1999**, *1*, 704
- [144] Schwartz, D.K., Schmeissner, M.L., Fendler, P.S. *J. Chem. Phys.* **1993**, *98*, 2558
- [145] Fendler, P., Goldmann, M., Schreiber, P. *Langmuir* **1999**, *15*, 1548
- [146] Fend, L., Fend, P., Goldmann, M., Moschowitz, C., Lohm, L. *Eur. Phys. J. B* **1998**, *6*, 1
- [147] Zuker, C., Benash, A., Ryan, J., Vothula, M., Brown, B. *Phys. Rev. B: Solid State* **1993**, *48*, 161
- [148] Personal-Interview with D. Fend, Chemical Technology Division in Argonne National Laboratories (February 24, 2000)
- [149] Spinks, J.W.V., Woods, R.J. *An Introduction to Radiation Chemistry*; Wiley Press: New York, 1980
- [150] Dugan, I.G., Dugan, E.D. *The Radiation Chemistry of Water*; Academic Press: New York, 1973
- [151] Welcome to Home, Peltier Cells and Applications <http://www.xlinc.com/peltier.htm> (accessed Feb 2000)
- [152] K Ray-Optical Systems Inc.- Products. <http://www.krayoptics.com/products.htm> Accessed Feb 2000

BIOGRAPHICAL SKETCH

Georgiy Wernadskiy was born in Colombia, St. Louis, on March 15, 1968. He was named after those boys who gave enough trouble to their mother. He was raised in Montana, and attended Melinda Vukobrat, Columbia, St. Louis. After his Advanced Level (High School third year) exam (August 1983), he was released to the Montana University, St. Louis, but all the universities were closed for approximately for ten years due to civil unrest in St. Louis. Searching for higher education made him come to Georgia College, Georgia, USA, on January 15, 1988 for his undergraduate studies. He received his Bachelor of Science from American Georgia College, Milledgeville, Georgia on June 15, 1990. He entered graduate school at the University of Florida on June 1990 and joined Professor Randy Gerner's Research group to work on his doctoral degree in analytical chemistry.

I certify that I have read this study and that in my opinion it conforms to acceptable standards of scholarly presentation and is fully adequate, in scope and quality, as a dissertation for the degree of Doctor of Philosophy.


Kenneth J. Duffin, Chairman
Associate Professor of Chemistry

I certify that I have read this study and that in my opinion it conforms to acceptable standards of scholarly presentation and is fully adequate, in scope and quality, as a dissertation for the degree of Doctor of Philosophy.


Richard R. Horsman
Professor of Chemistry

I certify that I have read this study and that in my opinion it conforms to acceptable standards of scholarly presentation and is fully adequate, in scope and quality, as a dissertation for the degree of Doctor of Philosophy.


David H. Howell
Assistant in Chemistry

I certify that I have read this study and that in my opinion it conforms to acceptable standards of scholarly presentation and is fully adequate, in scope and quality, as a dissertation for the degree of Doctor of Philosophy.


John E. Koryntak
Professor of Chemistry

I certify that I have read this study and that in my opinion it conforms to acceptable standards of scholarly presentation and is fully adequate, in scope and quality, as a dissertation for the degree of Doctor of Philosophy.


David O. Hunt
Professor of Chemical Engineering

I certify that I have read this study and that in my opinion it conforms to acceptable standards of scholarly presentation, and is fully adequate, in scope and quality, as a dissertation for the degree of Doctor of Philosophy.


Vincent T. Young
Associate Professor of Chemistry

This dissertation was submitted to the Graduate Faculty of the Department of Chemistry in the College of Liberal Arts and Sciences and to the Graduate School and was accepted as partial fulfillment of the requirements for the degree of Doctor of Philosophy.

May 2008

Dean, Graduate School